Spring 2009

Triple differential measurements of single and multiple ionization of argon by electron and positron impact

Jared M. Gavin

Recommended Citation

TRIPLE DIFFERENTIAL MEASUREMENTS OF SINGLE AND
MULTIPLE IONIZATION OF ARGON BY ELECTRON AND POSITRON
IMPACT

by

JARED MARTIN GAVIN

A DISSERTATION

Presented to the Faculty of the Graduate School of the

MISSOURI UNIVERSITY OF SCIENCE & TECHNOLOGY

In Partial Fulfillment of the Requirements for the Degree

DOCTOR OF PHILOSOPHY

in

Physics

2009

Approved by

Robert DuBois, Advisor
Jerry Peacher
Michael Schulz
Barbara N. Hale
Yanching J. Jean

ABSTRACT

Singly, doubly, and triply differential measurements of single and multiple ionization of Ar by 1 keV positron and electron impact have been measured for projectile energy losses from 0 to 200 eV, scattering angles of 0° to ±5°, and electron emission angles from 45° to 135°. For single ionization, both projectiles show similar overall energy loss distributions but differ with respect to varying scattering angles. Triply differential yields for the electron emission demonstrate the binary and recoil features but the lobes are distorted because of extraction field effects plus variations in grid transmission and solid angle as a function of the electron emission angle. Limited statistics and effects due to electric fields and solid angles mask observing definitive differences between positron and electron impact outside of error bars in the triply differential electron emission binary to recoil ratios. However clear differences in the magnitudes between positron and electron impact are observed. To study double ionization, ratios of double to single ionization, R2, were used. It was found that the doubly differential (DD) projectile and the singly differential (SD) electron emission ratios show differences in magnitude and intensity consistent with the expectations due to interference between a first order and a second order double ionization model. Triply differential (TD) electron emission double ionization ratios also exhibit a lower yield for positron impact, though the difference is much greater than that expected from interference effects.

ACKNOWLEDGMENTS

First and foremost, I must thank Mark Thomason for convincing me to attend graduate school, showing me the way through it and listening to all of my complaining. I must thank my Mother for being a mother in every sense of the word and my Father for always believing in me no matter how much I didn't. I must thank Jane Izzo for her love, her support and my precious son, Russell. I would not be the same person today without my sister Lacy and my brother Matthew. I must thank Phillip Hammons for being a legendary friend and ally against boredom. I must thank Dr. DuBois for giving me a research position, though I barely knew how to use a voltage meter, and for not holding my hand. I must thank Brain Swift, Russ Summers, and Charlie McWhorter for building and making my stuff work. I must thank Brian Tooke, Julie Cook, Jason Alexander and Aaron Laforge for all of their grad school shenanigans and for lending an extra set of hands. I would like to thank Dr. Peacher, Dr. Schulz, Dr. Hale and Dr. Jean for taking the time and effort to serve on my graduate committee. I will also not forget to thank Dr. Sayyar, Dr. Abedi and Mr. Guenter for telling me not to be lazy and for being friends as well as advisors. Last but definitely not least, I would like to thank God for his footprints in the sand.

TABLE OF CONTENTS

LIST OF FIGURES

LIST OF TABLES

1. INTRODUCTION

1.1. OBJECTIVE AND MOTIVATION

This work focuses on the fully differential measurement of ionization of argon by electron and positron impact and the differences that arise as a result of the particle-antiparticle relationship between the electron and positron. Not only does this type of study provide valuable understanding of matter/anti-matter interactions, the positron's opposite charge makes it the ideal particle for comparison to electrons in searching for charge effects on fundamental theories of atomic physics. Unlike comparisons of proton and electron impact where charge and mass both play a role, positron and electron impact comparisons isolate charge differences by removing the ambiguity introduced by mass differences.

Triply differential measurements for single ionization are measurements in which the energies and scattering- and emission- angles of the projectile and emitted electron are known, thus providing complete kinematic information about the interaction. Triply differential measurements for electron impact ionization have been available since the late 1960's [1], while the first ionization triply differential cross section (TDCS) for positron impact wasn't presented until 1998 [2] and was only for 0° scattering on H_2. The approach used in this work allows for doubly and triply differential comparisons to be made over a broad range of energy losses, scattering angles, and electron emission angles. Plus, by using position sensitive detectors in conjunction with time-of-flight (TOF) techniques, the present experiment diverges from traditional kinematic measurements by also resolving the degree of ionization. These comparisons provide

new insights and more sensitive tests of theory for the study of positron–atom interactions.

To place the findings of this work in context, understanding matter-antimatter interactions is important to many applications and understanding important aspects of physics. Positron Emission Tomography (PET) is being used extensively as a medical imaging technique in critical fields such as oncology, neurology, and cardiology. Experiments involving positron surface phenomena carry over into semiconductor technology as a means of scanning defects in solids and thin films. Triplet positronium (Ps) lifetime measurements provide crucial testing of QED, and positronic bound state properties and anti-hydrogen studies offer additional, tangible support for the CPT theorem. Therefore, further understanding of positron interactions with matter is important both practically and philosophically.

1.2. MEASURMENT BASICS

The present study is concerned with ionization of argon and how the ionization kinematics differ for positron and electron impact. By performing highly differential measurements of the scattered particle and the ionized electron, the kinematics for single ionization are studied in great detail. In addition, information about the electron emission and interaction mechanisms is obtained for double ionization. Argon has a valence configuration of $3s^2 3p^6$ with first, second, and third binding energies of 15.76, 27.62, and 40.89 eV. This means that a projectile must lose a minimum of 15.76 eV to eject one electron, and an additional 27.62 eV to eject a second electron. Hence, a positron or electron projectile must lose a minimum of 43.38 eV in order to directly eject two electrons from the M shell of Ar. The L shell ionization threshold is approximately 250

eV and therefore is much less probable plus it lies outside the range for the data presented here.

Consider a beam of positrons passing though and ionizing a dilute gas. For single ionization, the interaction kinematics are completely defined if the energies and angles (or momentum components) of two of the final state products are known, e.g., E_p, θ_p, φ_p; $\varepsilon_e, \theta_e, \varphi_e$ for both the scattered positron and the ejected electron. The coincidence signal for detecting both of these particles, $N_{p,e}(E_p, \theta_p, \varphi_p; \varepsilon_e, \theta_e, \varphi_e)$, is given by:

$$N_{p,e}(E_p, \theta_p, \varphi_p; \varepsilon_e, \theta_e, \varphi_e) =$$

$$\frac{d^5\sigma}{dE_p d\theta_p d\varphi_p d\theta_e d\varphi_e} N_p N_T \, \eta_p t_p \eta_e t_e \, \Delta E_p \Delta\theta_p \Delta\varphi_p \Delta\theta_e \Delta\varphi_e \qquad (1)$$

Here N_p and N_T are the number of projectile particles and target atoms, ΔE, $\Delta\theta$, $\Delta\varphi$ are the energy and angular ranges that are detected for the scattered positron and ejected electron, while η and t are their respective detection and transmission efficiencies. The differential probability for the coincidence event, σ, is fivefold differential since the ejected electron and scattered positron energies are related by $E_p + \varepsilon_e = E_o - IP$, where E_o and IP are the initial energy of the positron and the first ionization potential of the atom. However, for historical reasons this cross section is commonly referred to as the triply differential cross section.

Total cross section (TCS) measurements of ionization are where the total yields of either the scattered positron or the ejected electron are measured regardless of any post collision parameters. They represent the least sensitive test of theoretical models. Therefore, it is necessary to perform differential measurements in order to obtain a deeper understanding of ionization kinematics. Differential simply refers to the dependency of the measurements upon one (singly), two (doubly), or three (triply, also called fully and

e-2e in the case of single ionization) collision parameters. Singly differential measurements are where the ionization yields are measured as a function of only the energy or the solid angle (θ,φ) of one of the particles. Doubly differential measurements measure the yields of one of the particles as a function of two parameters, e.g., energy and solid angle. In both cases, the above equation must be integrated over the energies and angles of the undetected particle. The triply differential quantity represents the most sensitive test for theoretical models because it measures all of the parameters for each of the particles.

With regard to collision dynamics, when two objects collide, conservation of momentum dictates the scattering angles and energies of the objects post collision (Fig. 1.1). However, because of the opposite sign of the Coulomb force, electrons ionize Ar by repelling the bound electrons while positrons attract the bound electrons.

Once an Ar atom has been singly ionized, there are three bodies produced, the emitted electron, the projectile, and the Ar^+ ion. In cases where the projectile interacts primarily with the bound target electron and the target nucleus acts merely as a spectator, the interaction is referred to as being binary and two-body kinematics determine their energies and angles, e.g., $\vec{k}_i = \vec{k}_f + \vec{q}$ where k_i and k_f are the initial and final momenta of the projectile and q is the momentum transferred to the ejected electron. Along the beam direction, conservation of linear momentum means that the parallel component of the momentum transfer, q_{par}, is positive; the component transverse to the beam direction, q_{perp} must be in the opposite direction to that which the projectile is scattered. This means that a free, stationary, target electron must be ejected in the q direction; it cannot go
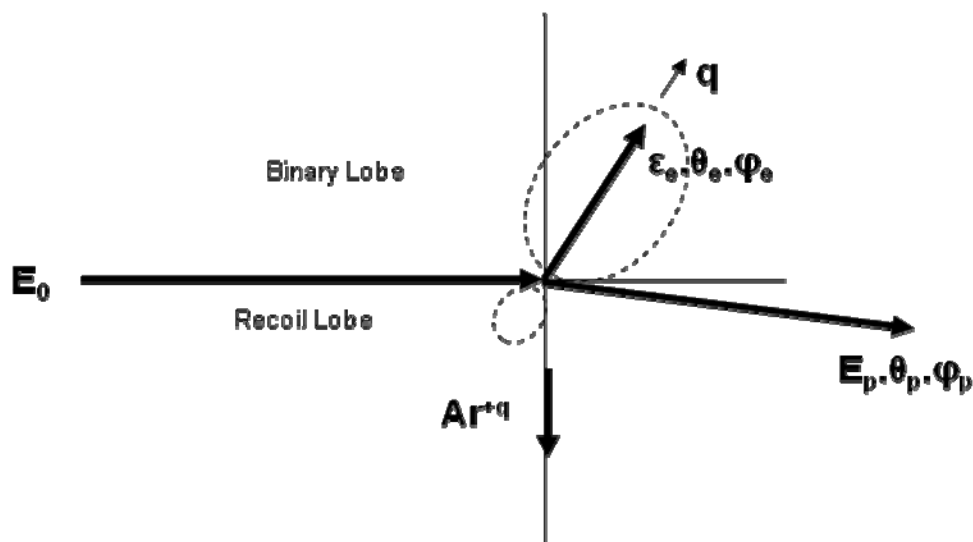
Figure 1.1. Three Body Kinematics of Single Ionization of Ar.

backwards. For bound electrons, due to the uncertainty in their momenta, instead of a well defined ejected electron angle for a fixed projectile energy loss and scattering angle, a range of momentum transfer magnitudes and angles occurs, i.e., a binary lobe. In the situation where the target ion plays a larger role, the emitted electron is turned around such that it ends up in the same "scattering" hemisphere as the scattered projectile. Plus, since it is turned around, it has the possibility of traveling in the backward direction with respect to the initial projectile direction.

Therefore, binary and recoil lobes are expected in the resultant post impact trajectories [1] if the scattered projectile and the ejected electron are both detected. As was stated, the binary lobes will be found in the forward hemisphere and in an opposite direction to that in which the projectile was scattered. In contrast, the recoil lobes are found at backward angles in the opposite direction of the binary lobes. It is also important to remember that pure two-body kinematics means that the binary lobe will be

centered on the q direction. Any deviations from this generally imply that subsequent interactions are taking place after the collision.

It is also important to remember that binary and recoil interactions have different probabilities and that the probabilities depend on the ejected electron energy (i.e., the projectile energy loss). Different probabilities for binary and recoil events also are manifested in the scattered projectile spectra where scattering in one direction can be more or less probable than scattering in the other direction. This is in contrast to measurements where the ejected electrons are not measured. In this case, Formula 1 must be integrated over all possible ejected electron angles and symmetry with respect to the projectile scattering is expected. By measuring coincidences between the scattered projectile and the ejected electron the symmetry is broken.

In the present experiment, the ejected electron detector is located above the beam axis. Thus the signature for binary interactions is a downward scattered projectile since the detected electron has been emitted in the upward direction. Likewise a signature for recoil interactions is an upward scattered projectile in coincidence with an upward emitted electron. This reasoning provides a method of mapping the electron emission of momentum transfer in which all kinematical information is known. Primary objectives of this work are to measure and compare the ejected electron lobes and the projectile scattering angles for positron and electron impact and to do this for a range of energy losses (ejected electron energies).

1.3.   POSITRON IMPACT IONIZATION BACKGROUND

Early positron-gas scattering experiments measuring total cross sections (TCS) were conducted throughout the 1970's and early 1980's by several groups using varying

techniques centered around beam attenuation though a gas cell. Many involved the use of magnetically guided beams. However, typical differential ionization studies require an environment free of magnetic fields. Also, a degree of ambiguity is introduced when searching for specific differences in ionization due to the contributions from other scattering processes in the TCS. A detailed review of these TCS measurements can be found in M. Charlton [3].

Beginning with the use of positron-He$^+$ time correlations by Fromme [4] for measuring total ionization cross sections from threshold to 1 keV, ionization measurements persisted through the 1990's and to the present becoming more differential [5-8] , innovative [9], and being measured for several inert gas targets [5, 8-20] as well as atomic hydrogen [11,22]. Most of the advances in positron ionization studies have focused on the low to intermediate impact energy regime (~ 0.5 to 500eV) and have inspired several theoretical treatments. A thorough review of the state-of-the-art for low energy positron interactions can be found in the review of Surko. [23]

1.3.1. Total Cross Sections. By far the majority of positron based studies have been measurements of total cross sections. Despite the accomplishments of the recent decades, questions still remain as to the time evolution of the Coulomb forces pertaining to many body interactions which are in some instances greatly influenced by particle properties as simple as charge and mass. Differences in total ionization cross sections arising from target polarization [24], electron capture by positrons [25, 26], and exchange interactions by electrons, in which positrons are excluded by the Pauli exclusion principle, create a demand for more rigorous theory [27, 28, 29] at lower energies where the first order Born approximation fails to agree. However, at higher impact velocities,

e.g., 1 keV, the Born predictions for TCS merge with experimental measurements for positron and electron impact ionization. This merging is expected because of the Born proportionality to charge squared and the lack of contribution from the Ps channel [10]. On the other hand, the merger may not always be accurate since absolute cross section measurements of single ionization by Cavalcanti [30] show differences in electron and proton impact for larger Z targets, though no significant differences beyond experimental uncertainties in the case of argon.

Going beyond single ionization, double ionization is understood to occur through three main mechanisms at higher impact velocities. One process involves a single projectile interaction with a bound electron and the subsequent liberation of a second electron by the outgoing first ejected electron. This is typically called the TS1 (two-step, one interaction) process. Another is the TS2 process (two-step, two interactions) which is the result of two projectile interactions, one with each ejected electron. The third process is called shake-off (SO) in which one electron is ejected directly by the projectile and a second electron is ejected due to ion state relaxation in response to the rapid loss of the first ejected electron. Observed differences between positron and electron impact double ionization at energies less than 1 keV were first suggested to arise from the interference between these three processes [31].

The interference arises because the cross section is proportional to the square of the sum of the amplitudes of the various double ionization channels, i.e., to $\left| \Sigma (TS1 + TS2 + SO) \right|^2$. In each case, the amplitude is proportional to the Coulomb force integrated over the collision time. Thus the cross section is proportional to $\left| \Sigma(F_{TS1}{*}time + F_{TS2}{*}time + F_{SO}{*}time) \right|^2$, where F, the coulomb force, is proportional to q, the

projectile charge times e, the ejected electron charge. For single ionization, $\sigma \sim \left| F \right|^2$. Therefore electron and positron impact yield identical cross sections. The TS1 and SO amplitudes are both first order interactions and therefore proportional to F while the TS2 process is a second order interaction which is proportional to $\left| F \right|^2$. The combination of these processes, i.e. $\left| \Sigma(F^*time) \right|^2 \sim \left| F_{1order} + F_{2order}^2 \right|^2 \sim \left| F_{1order} \right|^2 + 2Re\, F_{1order*}F_{2order}^2 + \left| F_{2order} \right|^4$, yields an interference term, $F_{1order}F_{2order}^2$, which is proportional to $(qe)^3$ and therefore charge dependent. Plus, since qe is positive for negative q and negative for positive q, the positron impact cross section is expected to be smaller than the electron impact cross section.

This explanation was later supported by Anderson [32] and Charlton [33] who measured ratios of double to single ionization (R2) for proton and anti-proton impact and for electron and positron impact, respectively, on helium. In addition, differences between electron and positron impact triple ionization of Ar have been interpreted in terms of nuclear attraction (repulsion) of the electron (positron) resulting in a subsequent acceleration (deceleration) and therefore larger (smaller) cross sections [34]. Inner-shell ionization could contribute to double ionization as well [32] but the probability is not large enough to account for the entire difference [35]. More recently, the R2 ratio was revisited in Kara [36] which upheld the suggestion of Helms et al. [35] that at sufficiently high energies, the charge dependence of double ionization vanishes due to the dominance of a single mechanism and the increasing importance of inner shell ionization for higher Z targets [18, 37]. DuBois [38] also showed larger charge state fractions for double and triple ionization of Ar for electron impact below and equal fractions above the inner L shell ionization threshold.

1.3.2. Single Differential Cross Sections. Single differential work for positron impact includes theoretical treatments in Schultz [39] and K. Bartschat [27] and measurements in Finch [40] and Falke [5]. Classical Trajectory Monte Carlo (CTMC) calculations of 100 eV electron and positron impact on He predict post collision interaction (PCI) effects on the electron emission resulting from the opposite projectile charges [39]. The positron attraction of the ejected electron increases forward scattering of electron emission as compared to electron impact. A distorted wave (for the projectiles), close coupling (for the ion and electron emission) hybrid computational model that yields close agreement with recent TCS experimental data predicts smaller single differential cross sections (SDCS) for energy loss from 68 eV positron impact ionization on Ar than for electron impact [27]. While this sophisticated model has the ability to account for projectile-target interaction, the lack of more highly differential experimental data prevents further testing.

Differential measurements of elastic scattering of low energy positrons at 60° by Ar presented in Dou [41, 42] showed structure in the impact energy range 55–60eV and was attributed to coupling between Ps formation, ionization, and elastic scattering channels. This structure was later refuted after similar measurements at 60, 90, and 120° across the same impact energy range found a constant intensity leading to a monotonic decrease at higher energies, thus ruling out the existence of resonances in the elastic scattering SDCS for positron–rare-gas collisions [40]. No such studies or analysis exist for the ionization channel.

The ability to distinguish a scattered projectile from an emitted electron which is possible for positron impact but not for electron impact ionization allowed Falke [5] to

separate angular measurement of projectile scattering from electron emission of Ar and Kr. These SDCS were used to invalidate the suspected involvement of classic Thomas scattering at 45° in the transfer of emitted electrons to positron projectiles.

Most recently, singly differential measurements of in-plane emission of Ar by 500 eV positron impact revealed constant double- and triple-to-single ratios for forward emission (45° - 90°) and increasing ratios with respect to increasing backward emission (90° - 135°) indicative of emitted electron-recoil ion interactions [43]. Backward double ionization emission ratios were shown to increase at approximately twice the rate of the triple ionization emission ratios.

1.3.3.   Double Differential Cross Sections.

1.3.3.   **Double Differential Cross Sections.** As positron impact ionization measurements become more differential, the use of larger targets to counteract low positron beam intensity becomes prominent in spite of the desire for more theoretically manageable targets such as H and He. Hence, the target Ar has been used in most positron impact double differential cross section (DDCS) measurements [6, 7, 44]. A major focus of these measurements was the search for electron capture to the continuum (ECC) where the emitted electron has nearly the same velocity as the outgoing positron projectile and in such a case it can be considered to have been transferred to a continuum state of the positron. This phenomenon is well documented for electron [45, 46] and heavy positive ion impact [47 - 49] by the observance of an anti-cusp and cusp, respectively, near the equi-velocity point in the electron emission or projectile energy loss spectrum. These findings along with preceding theoretical predictions [50, 51] prompted the DDCS calculation of Mandal [52] for positron impact on H which found a distinct cusp similar to those for heavy positive ions in the energy loss spectrum of

forward emission. Similar calculations for Ar using a CTMC model described a ridge like ECC structure in contrast to a cusp [53].

The ridge, instead of a sharp peak, was attributed to the low mass and expected larger angular scattering of the positron as opposed to the near straight final trajectory of heavy ions. Moxom [44] later provided support for the ridge like structure through the use of a magnetically guided positron beam incident on Ar in the first DDCS measurement for positron impact. While the latest experimental [19] and theoretical [54] attempts to find evidence of ECC consistently agree upon the idea that a wider disbursement of positrons results in a smeared, ridge-like ECC structure, disagreement is found with respect to a lower, experimental double differential cross section for positron energy loss above 70 eV at 30° positron scattering.

Aside from ECC and in comparison to electron impact, a definite increase in forward electron emission by positron impact on H and Ar is observed [6], as well as an increase in the production of low energy electron emission by positron impact on Ar [54]. Projectile energy loss DDCS measurements of 750 eV positrons scattering into a forward 17° cone from single ionization of Ar show excellent agreement with distorted wave Born calculations [38].

1.3.4.   Triply Differential Cross Sections. A major interest in positron impact studies has long been to experimentally compare triply differential cross sections (TDCS) for positron and electron impact. Typically the interest centers on comparing the magnitudes and directions of the binary and recoil lobes for the electron emission. Many years ago TDCS calculations using a second Born approximation with an improved target continuum-state wave function and neglecting Ps formation were performed for 600 eV

positron and electron impact ionization of He [55]. The kinematic parameters used were 4 and 8° projectile scattering for emission energies of 2.5 and 10 eV. Electron impact results had good agreement with the experimental data of Jung [56] and showed improvement over the unmodified second Born approximation through a decrease in the binary intensity and an increase in the recoil intensity. The positron impact calculations displayed more binary and less recoil intensity compared to electron impact. In addition, with respect to the momentum transfer direction, the binary and recoil emission was shifted closer towards (farther away from) the beam axis for positron (electron) impact. Both projectiles resulted in increased binary to recoil ratios at maximum intensity as a result of increasing momentum transfer. M. Brauner later indicated that the long range Coulomb, PCI method of Sadhanna Sharma and M. K. Shrivastava [55] was appropriate for TDCS of a few hundred eV impact energies by employing an exact, parameter free solution that satisfied three body Coulomb wave boundary conditions [57]. This parameter free approach also exhibited slow convergence of the first Born approximation at 2000 eV impact energy on H.

The first experimental TDCS measurements for positron impact were carried out for 100 [2] and 50 eV [58] impact energy on H_2 but were limited to scattering and emission at zero degrees. They showed conclusive evidence for ECC which had evaded earlier DDCS studies. These measurements were taken using a series of parallel plates to separate forward scattering projectiles from the electron emission and to act as an energy analyzer for the emitted electron [2]. While the initial measurement yielded excellent agreement with theory [2], subsequent measurement [58] after incorporating time-of-flight focusing of electrons entering the energy analyzer at different angles resulted in a

1.6 eV shift of the cusp toward lower energies from theoretical predictions [59]. The shift was attributed to an undetermined non-ionizing process leading to the additional energy loss.

Finally, the most recent triply differential electron/positron comparisons have gone beyond 0° scattering and single ionization, and found distinct differences in emission at 500 eV impact energy [60]. The work of this dissertation uses improved methods and extends that study to higher energies.

In recent years, triply differential measurements have continued for electron and ion impact [61-68]. The (e,2e) measurements of Taouil et al. [68] indicate that several improved first Born approximations fail to describe the asymmetry of the TDCS with respect to the momentum transfer at 0.5 au and suggests that a new, multi-step mechanism addressing the ion-electron interaction is necessary for better agreement. A similar (e,2e) study for the molecular target N_2 also shows discrepancies between calculations and measurements as to the symmetry about the momentum transfer direction and the intensity of recoil interactions as well [66]. However, a later triply differential study of 1000 eV electron impact on Mg shows good agreement between experiment and a distorted wave Born approximation (DWBA) model attributing success to the models ability to handle multiple scattering effects [61].

Fully differential measurements of slow (75 keV/amu) ion-impact on He imply that projectile–residual-target-ion interactions, not observable for electron impact, are more important than PCI between the emitted electron and projectile [67]. Velocities of this magnitude require electron, or positron, beams below 40 eV which are experimentally challenging. Also, ion impact study techniques typically involve the

measurement of the recoil ion- and ejected electron momentum, RIMS [67] or

COLTRIMS [62, 64], in contrast to this work. Projectile ions up to charge states of +18

have been used to study electron capture [62] and dissociative ionization of H_2 molecules

by proton impact have also been observed in full kinematical detail. An extensive

number of TDCS measurements exist for electron and ion impact in the references

mentioned above and the references therein.

1.4.   MODERATORS

One of the primary reasons that few highly differential positron impact studies

have been performed is that in contrast to electron and ion impact, only very low-

intensity positron beams are available to date. This is because positrons originate from

radioactive material through beta plus decay or the process of pair production. This

means that the majority of the positrons originally produced have large energies and are

lost in generating a well collimated, low-energy positron beam. Positrons may also

annihilate upon sufficient contact with an electron, emitting two, or three, photons that

obey conservation laws of energy, momentum. The study of positrons in the context of

atomic physics was restricted almost entirely to the measurement of positron annihilation

rates in atmospheric gases until the early 1970's. These efforts, along with others, lead to

the discovery of positronium and preceded the advent of moderating materials necessary

for the production of mono-energetic positron beams. Among these materials are MgO,

tungsten and more recently solid noble gas moderators. Moderators enabled the

investigation of processes such as elastic scattering, electronic excitation, ionization, and

vibrational and rotational excitation of molecules.

Because of its long half life and preferred positron production channel, ^{22}Na is the preferred radioactive material used in positron production. On the negative side, positrons emitted from ^{22}Na through beta decay have a broad range of energies in the hundreds of keV range. The positrons must be slowed down before a mono-energetic low-energy beam can be produced. This is done using various types of moderators made of materials which have a negative positron work function. Tungsten is one such solid and its use as a moderator has been employed and studied extensively. Tungsten is widely used because of its high positron work function and stability in high vacuum [69]. The effectiveness of a material as a moderator is generally defined by its efficiency (ε) which is the ratio of the number of extracted slow positrons to the total number of incident positrons upon the moderator. Once positrons enter a material, they undergo inelastic collisions and diffuse throughout the material. The difficulty in creating low-energy positrons lies in the affinity of the positron to annihilate with an electron. While a negative positron work function is highly favorable in preventing annihilation, structural defects within a material are highly unfavorable in that they cause the positron to become trapped and consequentially annihilate. Heating a material to sufficiently high temperature allows the atoms of the material to rearrange into a less defective and more crystalline structure. Impurities within the material also contribute to defects. Should the positron avoid becoming annihilated and return to the surface of crystalline tungsten, a small percentage of the positrons may be spontaneously emitted due to the negative work function of tungsten. Tungsten moderator efficiencies in the literature range from 10^{-4} to 1.2×10^{-3} [70 - 73]. Another method is to use frozen gases but they require a cryogenic environment for stability and that decreases their appeal. On the other hand, they have

higher efficiencies. For example, solid neon moderators have obtained efficiencies on the order of 7×10^{-3} [71].

As stated, heating the moderator to high temperatures is essential for removing defects and improving the crystalline structure. Tungsten has a melting point of 3422 C. Tungsten typically combines with oxygen to form a tungsten oxide. Tungsten may also combine with carbon to form tungsten carbides. Both oxygen and carbon counteract tungsten's negative positron work function, thus decreasing its moderating efficiency. Because of tungsten's high melting point, single crystalline tungsten is more difficult to produce and more expensive than polycrystalline tungsten. Polycrystalline tungsten of 99.9% purity and in the form of foils, mesh, and powder is quite common. Various methods and procedures have been employed to produce efficient moderators and most all include chemical etching, heat treatment, reducing contaminant exposure, increasing the effective moderating surface area, or a combination of the latter.

Chemical etching reportedly removes surface contaminants within 3 minutes and further etching reduces the thickness of the material [72]. Etching is typically done as a pretreatment leading to heating; however, etching post heat treatment preferentially removes the least stable atoms, such as those surrounding defects and in certain crystal faces [70]. H.M. Weng conducted etching by immersion of their tungsten samples into a chemical solution prepared by mixing 10 g NaOH, 10 ml ammonia (25-28%), 26 ml H_2O_2 (30%) and 54 ml distilled water [72]. M. Greiner and P. Kruse electrochemically etched in a 3 M NaOH solution using a platinum counter electrode and applying a constant voltage of 1.00 V for 15 minutes [70].

William D. Klopp, Walter R. Witzke and Peter L. Raffo conducted an extensive investigation of the mechanical properties and recrystallization of tungsten during and after heat treatment by arc melting and electron beam heating [74, 75]. The differences between these two methods are stated as follows. Arc melting involves rapid melting and high pressure exposure to the molten metal, while electron beam heating involves a slow dripping melt and low pressure exposure to the molten metal. Although the investigation did not include positron moderation, recrystallization rates and crystal grain growth induced by heat treatment were shown to be dependent upon not only the duration of the treatment and the amount of heat applied, but prior strain as well. This implies that the way various forms of tungsten are produced may influence the duration and temperature necessary to induce recrystallization. Joule heating is perhaps the most common way of removing imperfections and crystallizing tungsten. The heating of tungsten must be done in vacuum or in the presence of an inert gas due to its ability to oxidize. Inert gases serve as a vaporization retardant. This method involves transporting electric current through tungsten which creates heat because of the electrical resistance. Efficiencies up to 1.2×10^{-3} have been obtained by H.M. Weng using joule heating combined with chemical etching pretreatment [72]. Other heating methods include in situ heating [76], inert atmosphere furnace heating, zone refining [77], and magnetic induction.

The heat treatment used in the preparation of the 1.2×10^{-3} ε moderator was 20 minutes at 1600 C [72]. Other efficiencies on the order of 1×10^{-4} are reported in the literature [70, 71, 73] resulting from varying durations and temperatures. In regards to recrystallization, swaged electron-beam-melted tungsten was reported to be 73% recrystallized after 1 hour at 2300 F and fully recrystallized after 1 hour at 2400 F [74].

In the present study, joule heating of tungsten meshes confined between two tungsten strips was used. The experimental setup only allowed us to measure the moderated positron intensity at the end of the beamline. These data imply that our moderation efficiency was on the order for 1×10^{-4}.

The recrystallization is an important aspect of moderator efficiency but the geometry of the source and moderator also play a role. It is estimated that the reemitted positron energy distribution is broadened from a FWHM of 0.2 eV for foil to a FWHM of approximately 3 eV for mesh moderators [73]. This is attributed to the construction of the mesh with round wires as opposed to the flat surface of foil moderators and the positron's preferential reemission normal to the surface. Oxidation was also proposed to affect the broadening of the energy distribution as well.

2. EXPERIMENTAL SETUP

2.1. OVERVIEW AND POSITRON BEAM

The experimental apparatus in the present study consists of a positron source, tungsten mesh moderator, and beam optics followed by a gate valve, a small accessible compartment where the electron beam was injected, and finally an interaction chamber. Magnetic shielding filled with lead bricks for radiation shielding surrounded the source and beamline up to the gate valve. Additional lead bricks were positioned outside the magnetic shielding to further reduce the radiation field. All of this sat on a raised platform constructed of cinderblocks which provided radiation shielding below the source and prohibited access to this region. A wall of solid cinderblocks surrounded the entire area to an approximate height of 1.8 m for additional shielding and to prevent proximity to the source. Except for a small region where the positron beam entered the chamber, outside the shielding wall no radiation level above background could be detected.

A schematic of the entire apparatus is shown in Fig. 2.1. Positrons were emitted from a 6 – 7.8 mCi ^{22}Na source mounted on a vacuum micrometer in order to position it close to the moderator. The fast emitted positron energies were moderated by three layers of annealed tungsten wire mesh. The moderator was biased at 1000 V. Slow positrons emitted from the moderator have an energy equivalent to the product of their charge and moderator voltage. The source was biased 9 V positive with respect to the moderator while an extractor positioned immediately after the moderator was biased to extract a fairly parallel beam of positrons and establish an initial focal point (area). This was followed by an anode, a series of electrostatic lenses and a set of horizontal
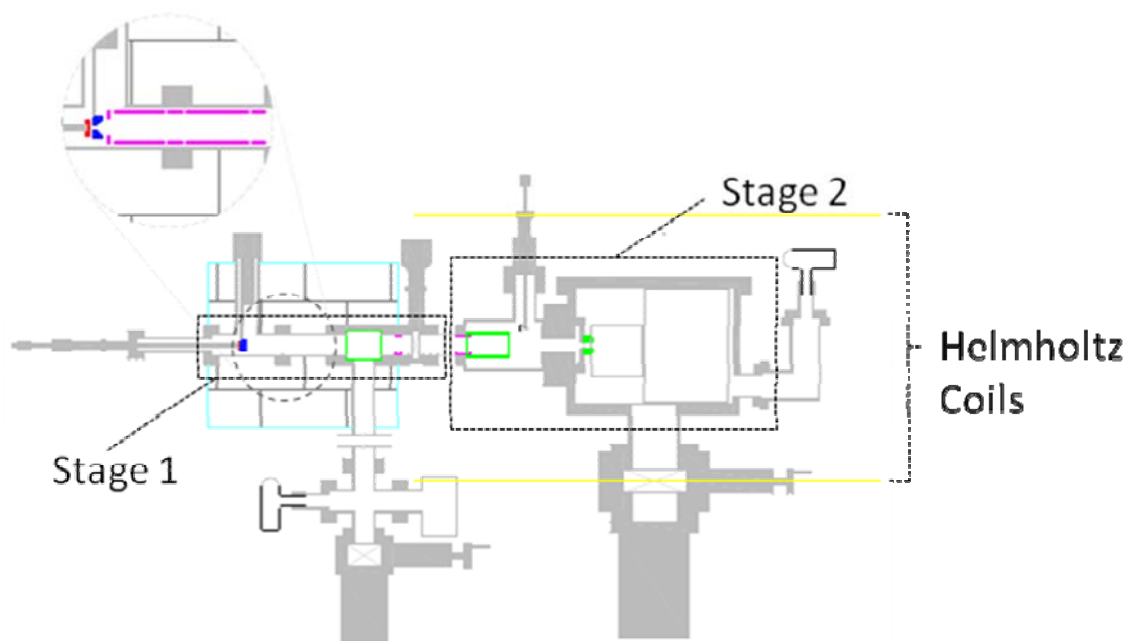
Figure 2.1.   Side View of Apparatus.

deflectors which bend the beam 15° toward the interaction chamber (Fig. 2.2). The

beamline was constructed of stainless steel ConFlat flange components. Just before the

interaction chamber, an additional lens and horizontal and vertical deflectors were used to

focus and steer the beam through a 3 mm aperture for electron impact or a 6 mm aperture

for positron impact. The larger aperture was used for the positrons in order to acquire a

higher beam intensity. A compartment positioned before the aperture housed the last lens

and deflectors and served as the insertion point for a channeltron and an electron gun.

The channeltron was mounted on a manipulator so it could be positioned on axis or away

from the beam. This "beamline" channeltron was used to obtain optimal focus and

intensity of the beam before passing through the aperture. After the aperture, beam rates

of 400–500 Hz and 1.5-5 kHz were obtained for positron impact and electron impact,

respectively.
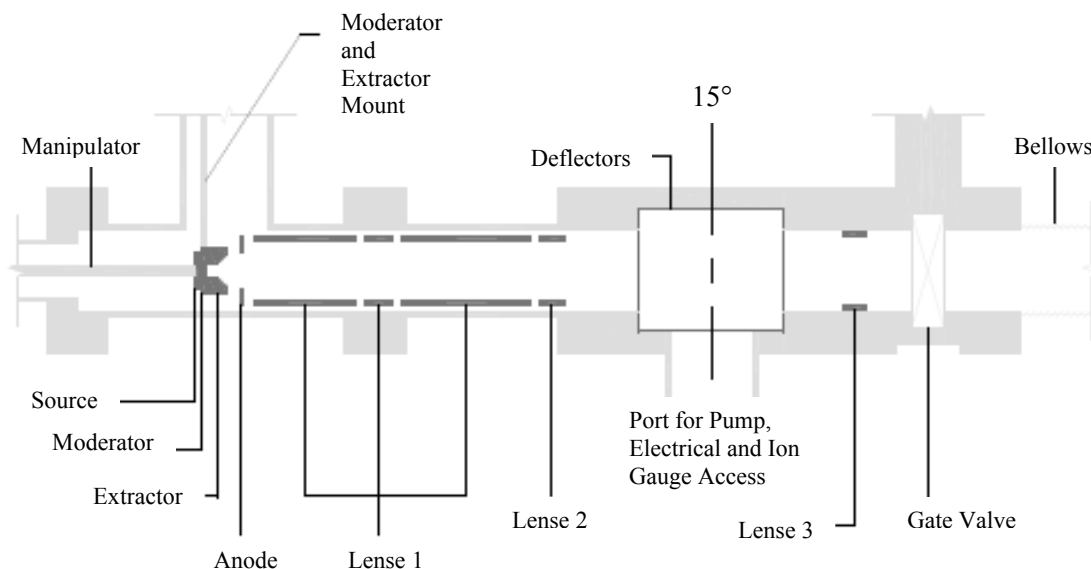
Figure 2.2.   Side View of Stage 1.

The beam line was evacuated through a 3.5 cm hole in the bottom of the 15° beam line deflector section by a Leybold Turbovac 50 turbomolecular pump backed by a Leybold Trivac D4A mechanical pump. Base pressures in the beam line and source region were in the low 10^{-6} Torr range. The turbo pump was mounted on a conflat cross which also accommodated an ion gauge tube and voltage feedthroughs for the transport optics.

2.2.   BEAM SIMULATION TESTS

Using SIMION 7 to simulate charged particle optics, a 3D model of the positron source and beamline was created to simulate the positron transport through the entrance aperture of the interaction chamber. This model served as a starting point in finding optimal transport voltages. The model was used to simulate any additions or modifications made to the transport and what effects they would have on the transport

efficiency. Positrons were simulated to come off of the moderator in a full 2π angular range and evenly across the diameter of the exposed moderator. Despite efforts to make the model accurate, the voltages used in the model typically differed from the actual optimal voltages used on the apparatus. Eventually, it was realized that the emission energy greatly influenced the trajectories and voltages used in the model. This could partially explain the discrepancy between the optimum voltages predicted by the model and actual voltages used. The discrepancy could also be due to the efficiency varying across the moderator. The model also showed that the 15° deflectors acted as a one-dimensional lens which diminished the ability to maintain a sharp focus at the input aperture. The loss of approximately two thirds of the count rate obtained on the beamline channeltron upon injection into the interaction chamber is attributed to these reasons. In Figure 2.3, three SIMION transport simulations are shown starting from the moderator to the interaction chamber entrance. Only two starting points at the extremity of the moderator were used so that the beam focus could be more easily observed. Initial starting energies of 0, 1.5, and 3 eV were used. These initial energies are within the range measured by Makoto Muramatsu et al. [65]. The same voltages were used in each simulation. A definite broadening of the beam can be seen by going from 0 to 1.5 eV, and at 0, 1.5, and 3 eV, the Simion simulation predicts a beam has transport efficiency of 100, 90, and 76%, respectively. This is much larger than could be achieved experimentally. After conclusion of this study, it was suggested that the lower injection efficiency we observed may be due to magnetic defocusing as the beam exits the magnetic shielding surrounding the beamline.
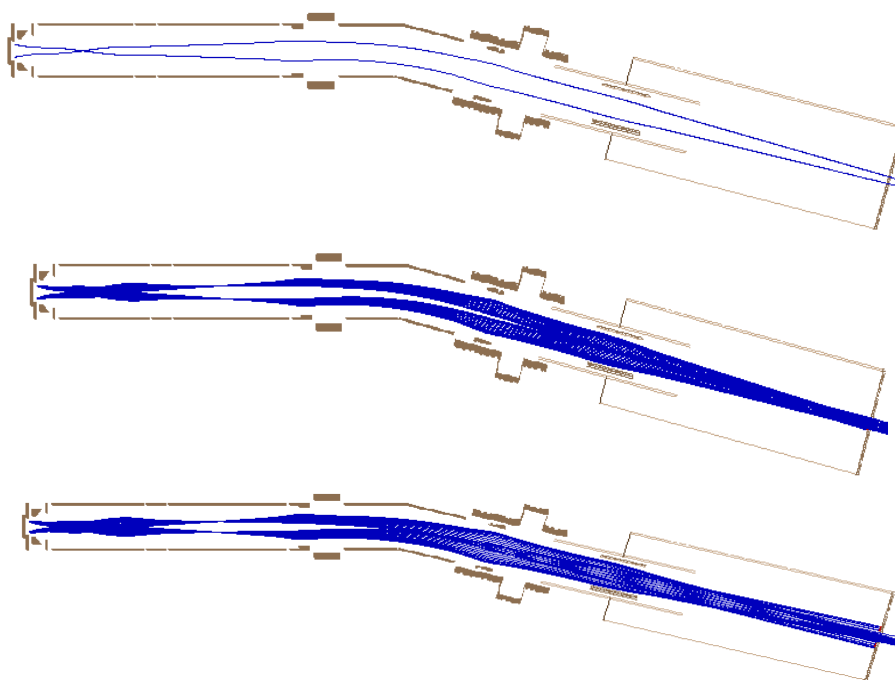
Figure 2.3.   Transport Simulations.

From top to bottom; 0, 1.5, and 3 eV initial energy. The moderator is located at the far left and the interaction chamber entrance is located at the opposite side.

2.3.   ELECTRON BEAM

For the electron impact experiments, electrons were produced using a simple electron gun mounted at the end of the positron beam line just before the entrance to the interaction chamber. The gun, plus a 90° cylindrical deflector attached to the end of the gun, could be moved horizontally and vertically with respect to the beam line and could be rotated in order to position it with respect to the entrance aperture or remove it in order to use the positron beam (Fig. 2.4).
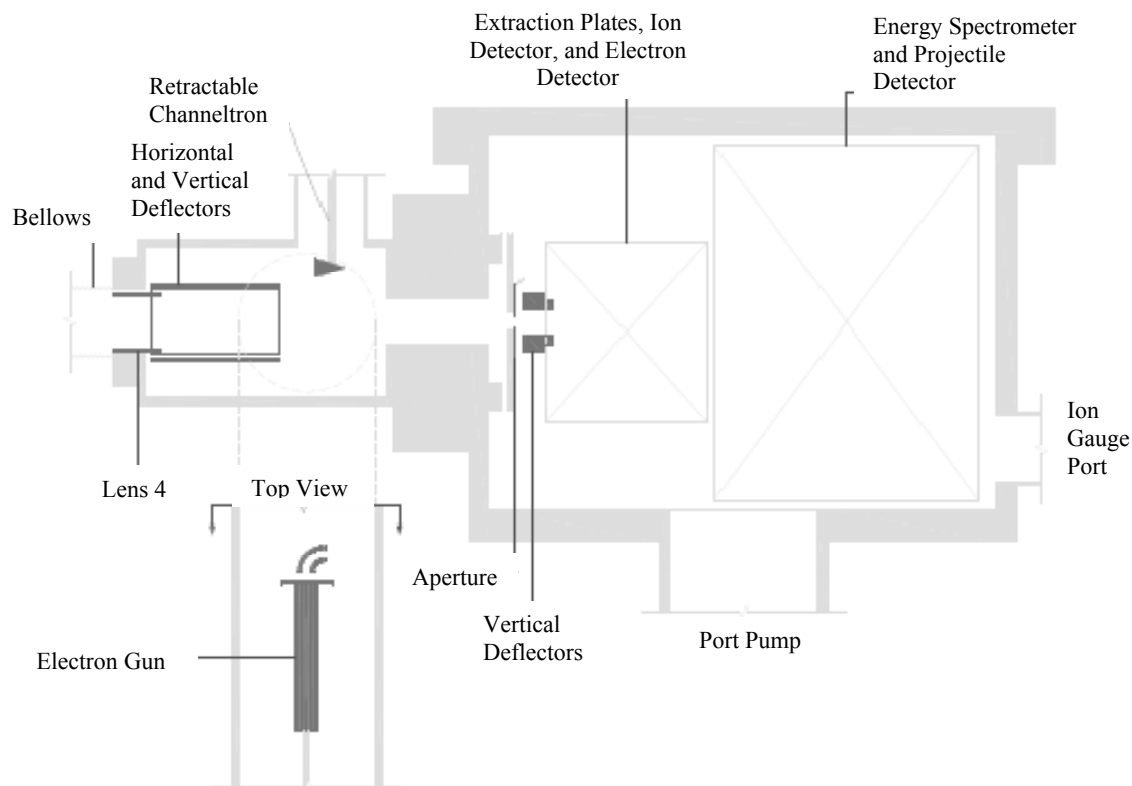
Figure 2.4.   Side View of Stage 2.

2.4.   INTERACTION CHAMBER

The interaction chamber houses an interaction region where the ion extraction and

electron emission are measured followed by a projectile energy spectrometer. Helmholtz

coils were positioned above and below the interaction chamber and used for nullifying

the earth's magnetic field. The interaction chamber was evacuated through a 15 cm hole

by a Leybold Turbovac 361 turbomolecular pump backed by an additional Leybold

Trivac D4A mechanical pump. The interaction chamber pressure was measured by an

ion gauge located more than 30 cm away from the closest detector and was not in direct

line of site of that detector. Typically, the chamber pressure was 3 x 10^{-6} Torr without target gas and 2 x 10^{-5} Torr with target gas.

2.5.   INTERACTION REGION

After passing through the aperture, the positron or electron beams pass between a set of vertical deflectors and intersect a gas jet target located between two biased horizontal plates (Fig. 2.5). The vertical deflectors are used to deflect the beams for testing purposes and are grounded during data acquisition. A target gas of 99.9% Argon (Ar) was injected perpendicular to the beam through a horizontal grounded needle. The needle had a diameter of 0.5 mm and its vertical position as well as its distance away from the beam axis could be adjusted from outside the chamber. The target gas pressure was controlled by a leak valve. The intersection of the beam and target gas defines the interaction volume where the target density is approximately 60 times higher than the chamber gas density while gas is being injected.

Scattered projectiles, ejected target electrons and target ions produced in the interaction region, where the beam intersects the target gas, are measured by two position sensitive detectors (PSD) and a channeltron detector. Each PSD consists of a front mounting plate with a stainless steel 78% transmission mesh, two 47 mm diameter multichannel plates (MCP) arranged in a chevron (v-like) arrangement, and a Roentdek delay line anode which are all surrounded by a grounded encasement.

Two 8.89 cm (3.5") square steel plates, one above and one below the beam path, each coated with soot for minimizing reflections and secondary electrons, were biased to produce an electric field used to extract target ions produced in the interaction volume. Plus 1.5 V was applied to the plate above and minus 2 V was applied to the plate below.
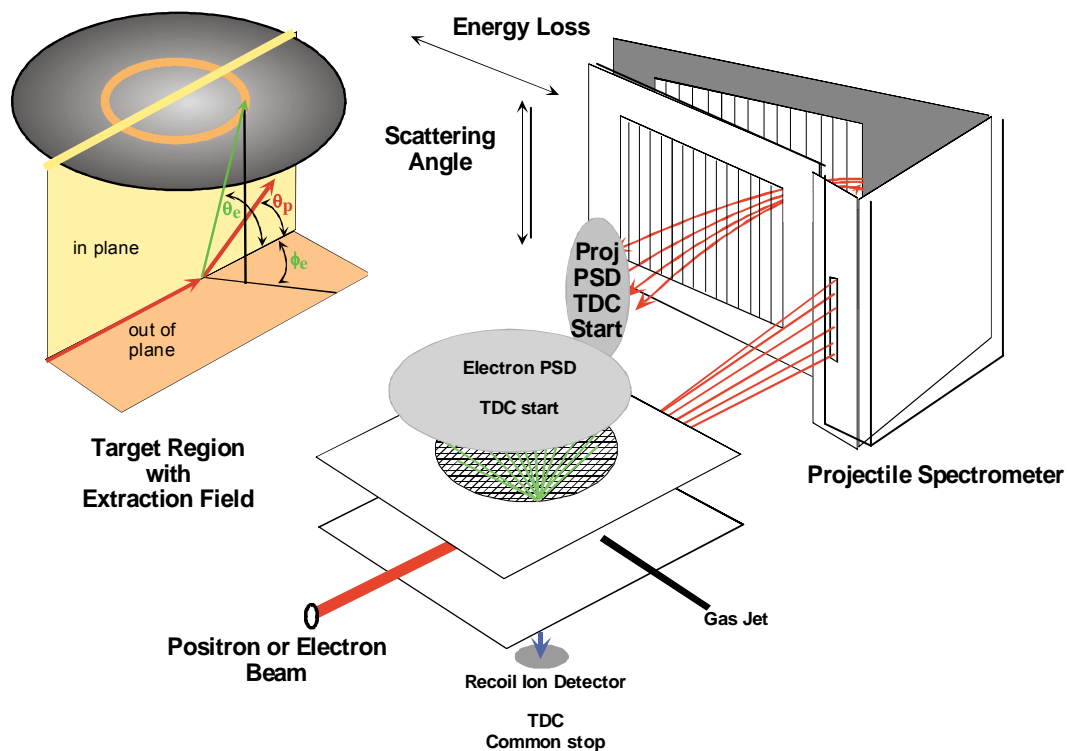
Figure 2.5.   Extraction Assembly and Energy Spectrometer.

The resultant 1.4 V/cm electric field extracted ions from the interaction region downward

through a 0.635 cm (0.25") diameter hole in the lower extraction plate into a drift region

followed by the channeltron detector. Emitted electrons could exit through a 5.08 cm

(2") diameter hole in the upper extraction plate and be detected by the electron PSD. A

stainless steel, 78% perpendicular transparency (SS78) mesh was spot welded across the

upper extraction plate hole in order to create a uniform extraction field in the extraction

region. The extraction plates are 2.54 cm (1") apart and the target needle is positioned

approximately 1.27 cm (0.5") above the bottom plate. The target needle extends from

beyond the edge of the extraction plates up to the edge of the 0.635 cm (0.25") diameter

hole in the lower extraction plate (Fig. 2.5).

2.6. EXTRACTION SIMULATION TESTS

Simion extraction simulations of target electrons emitted with energies of 1, 5, and 15 eV are shown in Figure 2.6 along with a field free simulation in which the both extraction plates are 0 V. Emitted electrons are simulated to emit in the scattering plane along the beam line every 5°. The 1 and 5 eV simulations are each divided into two illustrations; upward and downward scattering. As the emission energies decrease, emitted electron trajectories begin to deviate from the field free and 15 eV emission simulations behavior and are greatly influenced by the ion extraction field to the extent that very low energy electrons are completely turned around. Table 2.1 provides the detected position to geometric emission angle calibration of the simulations for the three different energies. The present data were not corrected with respect to the emission angles because though our energy losses are accurate, they contain a broad energy range and cannot be further dissected. Therefore, at a particular detector location 5 eV emission at a particular angle is indistinguishable from 1 eV emission at a different angle.

A SIMION ion extraction model was also used to simulate time and position focusing of the ions. Ion flight simulation also confirmed that Ar^+ ions with $20 - 40$ meV of energy or less originating from outside the direct line of sight of the recoil detector were undetectable which means that coincidences with recoil ions restricts the ionization events to the interaction region only. The effect of the grounded target needle on the emitted electron trajectories was found to be negligible with respect to forward and backward emission.
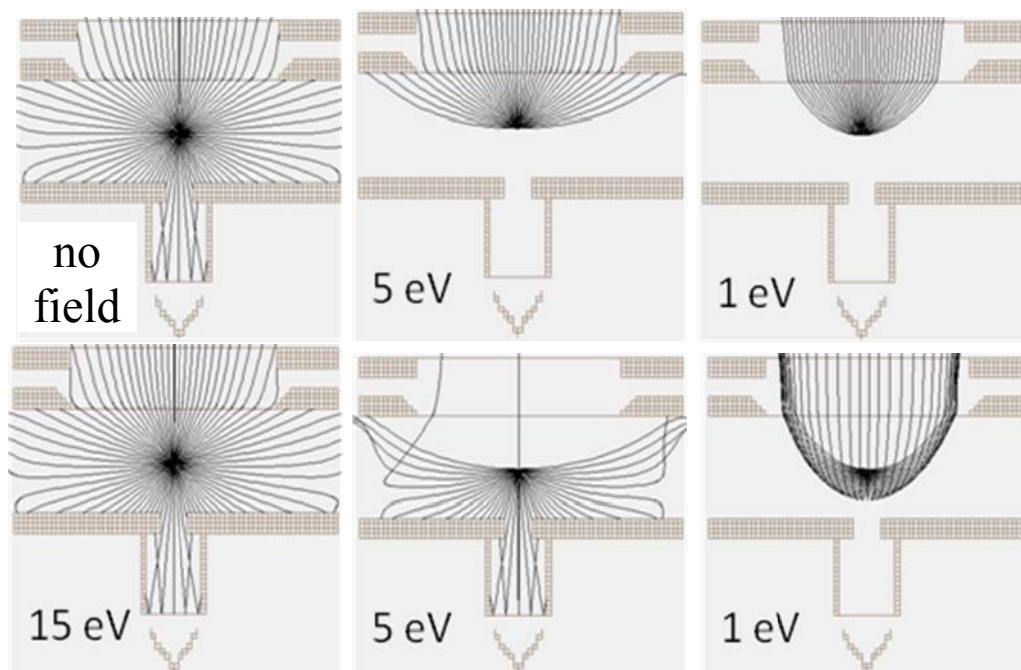
Figure 2.6. Extraction Field Simulations.

1, 5 and 15 eV electrons emitted isotropically in a 1.4 V/cm extraction field. Top; upward emission. Bottom; downward emission.

2.7. PROJECTILE ELECTRONICS

An electrostatic projectile energy spectrometer, equipped with a 2D channel-plate detector, was positioned directly in the beam path 0.318 cm (1/8") after the extraction plates (Fig. 2.5). A 0.508 cm (0.2") wide, 12.7 cm (5") height slit aperture coated with soot serves as the spectrometer entrance. This width and distance from the center of the interaction region equates to the acceptance of projectiles scattering between ±3.2° horizontally. The height of the slit extends beyond the upper and lower extraction plates which restricts the projectile scattering angles between -20° and +20°. However, the which restricts the projectile scattering angles between -20° and +20°. However, the scattering angles are ultimately limited to position and diameter of the projectile PSD. A

Table 2.1.   Observed vs. Actual Emission Angle.

Observed "geometric" versus actual emission angles for various emission energies.

Emission Angle (deg)	1 eV	5 eV	15 eV
	Observation Angle		
0	51		
5	53		
10	54		
15	56		
20	58	45	
25	60	47	
30	63	50	45
35	65	54	49
40	67	58	53
45	69	61	56
50	72	64	60
55	74	68	64
60	76	71	68
65	79	74	72
70	81	78	75
75	83	81	79
80	85	83	82
85	88	87	86
90	90	90	90
95	92	93	94
100	95	96	98
105	97	99	101
110	99	102	105
115	101	106	108
120	103	108	112
125	106	112	116
130	108	115	120
135	110	119	124
140	113	122	127
145	115	126	131
150	117	129	135
155	119	133	
160	121	135	
165	123		
170	125		
175	127		
180	128		

SIMION model of the energy spectrometer was used to determine the approximate distance traveled by the projectile from the center of the extraction region to the projectile detector. This distance is dependent on the horizontal scattering and was determined to be approximately 19 – 21.6 cm (7.5 - 8.5"). This distance along with the diameter of the projectile detector is used to calibrate the projectile vertical scattering angles. Therefore, the maximum measurable scattering angle is $7° \pm 0.4°$.

The projectile spectrometer was a specially designed "modified cylindrical spectrometer" which consisted of a small inner cylinder and an outer surface consisting of a flat back plate and side wall. The electrostatic field in the spectrometer is controlled by applying an inner attractive voltage to a 1/4 cylindrical piece (the inner plate) which is connected by a series of resistors to a one-dimensional vertical grid of wires along the spectrometer plate to which the projectile PSD is mounted. A repulsive voltage is applied to the outer spectrometer wall. The spectrometer is designed to focus horizontal scattering angles and distribute projectiles horizontally, according to their energy, across a PSD located at the exit plane. The vertical projectile scattering angles are preserved by the spectrometer field. The projectile PSD is centered vertically with the interaction chamber entrance aperture, the target needle and the beam. The deflection of the beam by the extraction field causes a shift in the zero projectile scattering position, but this is small and does not result in a loss of data.

2.8. COINCIDENCE ELECTRONICS

An electronics schematic is shown for signal processing in Figure 2.7. Inputs to eight 16 bit time-to-digital converters each having 500 ps resolution per channel, are 4 start signals, e.g., two horizontal-positions and two vertical-positions, acquired from each

PSD and a common stop signal from the recoil detector. The time differences between the individual starts and stop provide information about correlated and uncorrelated particles while the time differences between the two horizontal or the two vertical starts from a single detector provide information about the horizontal and vertical position of the detected particle. Cobold, a PC based data acquisition program from Roentdek GmbH, is used to display these coincidences in eight 1 dimensional plots referred to as time of flight (TOF) spectra. Coincidences associated with the interaction between the beam and target gas occur at a particular time difference and emerge as peaks in the TOF spectra. The peak positions are related to the mass and charge of the particles detected according to $q/m = d^2/(2Ut^2)$ where q is the ion charge, m is the mass of the ion (approximately 40 a.u. for Ar), d is the distance from the interaction volume to the ion detector (d = 3.81 cm), U is the electric potential difference (U = 3.5 V) and t is the time-of-flight. This relationship allows us to identify the peaks in the TOF spectra.

Furthermore, Cobold uses the horizontal and vertical times of flight from each detector to calculate the impact position on the detectors corresponding to each coincidence and generate 2D spectra. More details concerning Cobold spectrum generation and analysis will be discussed in the analysis section below.
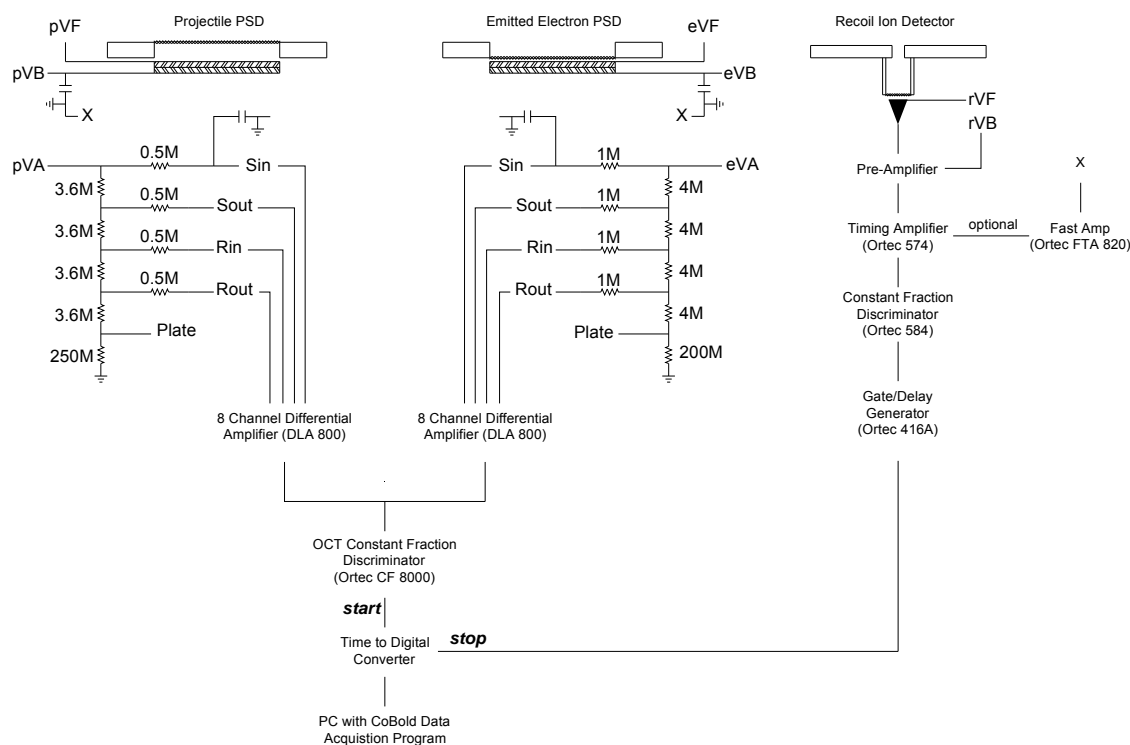
Figure 2.7.   Signal Processing Schematic.

Projectile (emitted electron) PSD front voltage; p(e)VF. Projectile PSD back voltage; p(e)VB.
Projectile (emitted electron) anode voltage; p(e)VA. Recoil ion detector front voltage; rVF.
Recoil ion detector back voltage; rVB. Mega ohms; M. Signal in and out; Sin and Sout.
Reference in and out; Rin and Rout. X; see Fast Amp at far right.

The electron PSD has a front bias of 225 V. It views the interaction region and

the beam path so it can detect photons, scattered and ejected electrons, plus scattered

positrons with sufficient energy to overcome this bias voltage. The energy spectrometer

voltages direct the high energy forward scattered projectiles, either positrons or electrons,

to the projectile PSD which has a front bias of -10 V to minimize the detection of low-

energy secondary electrons. The recoil detector has a -2.5 kV front voltage and hence

only photons and ions produced in the interaction volume or positrons which are

scattered by 90° can be detected and create a stop signal. If this stop signal is within a 16

μsec window from a start signal from the projectile or electron detector, a valid

coincidence event is recorded. Coincidences can also occur when both an emitted electron and a scattered projectile and a recoil ion are all simultaneously detected; this defines a triply differential coincidence. Coincidences associated with a particle produced in a different interaction do not occur at a specific fixed time and are referred to as background events. Coincidences associated with particles produced in the same interaction occur at particular times and are referred to as real events. See Figure 3.1 in a following section. For low signal rates, the background is low and constant and events appear as clear peaks in the TOF spectra. To keep the backgrounds low, proper precautions were taken such as coating the conductor surfaces with soot in order to reduce the scattered and secondary electron signals from these surfaces, insulating high voltage and signal cables, careful adjustment of the amplifier gains and discriminator settings and/or lowering the electron beam rate.

2.9.   MISCELLANEOUS TESTS

Before the data were recorded, various tests were performed to ensure the proper and intended functioning of the apparatus. A small light bulb filament near the interaction region was heated and used to create electrons for testing the detectors and electronics. Detector voltages and discriminator settings were adjusted by viewing the signals on an oscilloscope, noting the counting rates for each channel, and observing the percentage of "lost" signals using the Cobold data acquisition software. If a start occurred with a stop, this is called a "hit". Otherwise, the occurrence is called a "no hit". A histogram style spectrum where values of 1 and 0 were given to hits and no-hit, respectively, was created for each channel. This is a useful indicator of which channels need adjustment either in the amplifier gain or the discriminator level.

As a precaution for protecting the MCPs and the sensitive differential amplifiers, detector voltages were turned up incrementally and simultaneously. The PSD front detector voltages were positively biased by approximately 25 V with respect to a SS78 mesh grid immediately before the front MCP of the PSDs. The projectile PSD grid was set to -10 V to reject secondary electrons. These reduced the PSD background and prevented the loss of signal on the front MCP. The emitted electron PSD front voltage was set to 225 V for greater emission angle acceptance and a direct mapping of electron arrival positions between the upper extraction plate and the emitted electron PSD (Fig. 2.5).

Once the detectors were verified to be working properly, a beam was injected into the spectrometer for image positioning, image focusing and energy calibration. During this phase, projectile PSD stops were produced from the projectile PSD anode rather than from the recoil ion detector, and starts were produced from the projectile PSD MCP back plate and electronically delayed. For proper time sequencing, the stops were electronically delayed by 150 ns. The horizontal width of the 2D beam image provided information about the beam energy plus its horizontal diameter and the vertical width was a more accurate measure of the beam diameter. Comparing the detector image size in channels with respect to its known physical size, the beam diameter was determined. For positrons with a 6 mm aperture at the interaction chamber entrance, the beam had a FWHM of 6.2 mm upon contact with the detector. For electrons with a 3 mm aperture, the FWHM was 4.3 mm. This diameter could be extrapolated back to the interaction region to determine the interaction height and width. The projectile image height was also used to determine the scattering angle calibration and resolution, 0.13° per channel

from the vertical beam center. The scattered projectile energy calibration was performed by stepwise decreasing the beam energy and observing the distance the image shifted. This calibration was determined to be approximately 4 eV/channel for both positron and electron projectiles.

Using a higher intensity electron beam, the magnetic field and extraction field were adjusted to maximize the recoil count rate. For typical beam intensities and target pressures given above, triply differential single ionization (TDSI) coincidence rates were on average 3/hr for positron impact and 125/hr for electron impact. Total TDSI coincidences recorded for positron and electron impact are approximately 11,000 and 35,000, respectively. Because of the low signal rates during the data accumulation, it is assumed that maximum recoil count rate is the result of maximum overlap between the beam, target gas, and the column extrapolated from the recoil detector and aperture alignment. Total recoil counts were not recorded due to the diminishing effect on accuracy by fluctuations of dark counts and/or electronic noise over a period of months in the case of the positron data.

3. ANALYSIS

3.1. SPECTRA AND BACKGROUND GENERATION

Data analysis was performed in a comparative fashion with electron and positron impact data taken under practically identical conditions such as chamber pressure, detector efficiencies, SS78 mesh grid transmission, and experimental voltages and geometry. The data are recorded in hex code in a list mode fashion using Cobold software. The listmode data can then be resorted at a later time into spectra using various conditions. Primarily the ejected electron-recoil ion and the scattered projectile-recoil ion coincidence data were resorted into 1D TOF spectra and 2D spectra. The words "ejected" and "emission" are used interchangeably in reference to electrons originating from the target, and the word "scattered" is used in reference to ionizing projectiles. Abbreviations such as P1 and E1 are used to notate the various types of coincidences and combinations with the letter or letters referring to the coincidence partner to the recoil ion and the number designating the degree of target ionization e.g., P1 indicates scattered projectile spectra for single ionization, E1 ejected electron spectra for single ionization, (Table 3.1). Also, SD, DD, and TD will be used interchangeably with singly, doubly and triply differential, respectively.

3.1.1. TOF Spectra. The TOF spectra (Fig. 3.1) distinguish "real" and "random",i.e., correlated versus uncorrelated, events. The real events are seen as peaks which identify the degree of ionization, i.e., the number of electrons removed from the target, plus distinguish target gas ions, e.g., argon ions, from background gas ions, e.g., molecular nitrogen and oxygen plus any atomic fragment ions that they can generate.
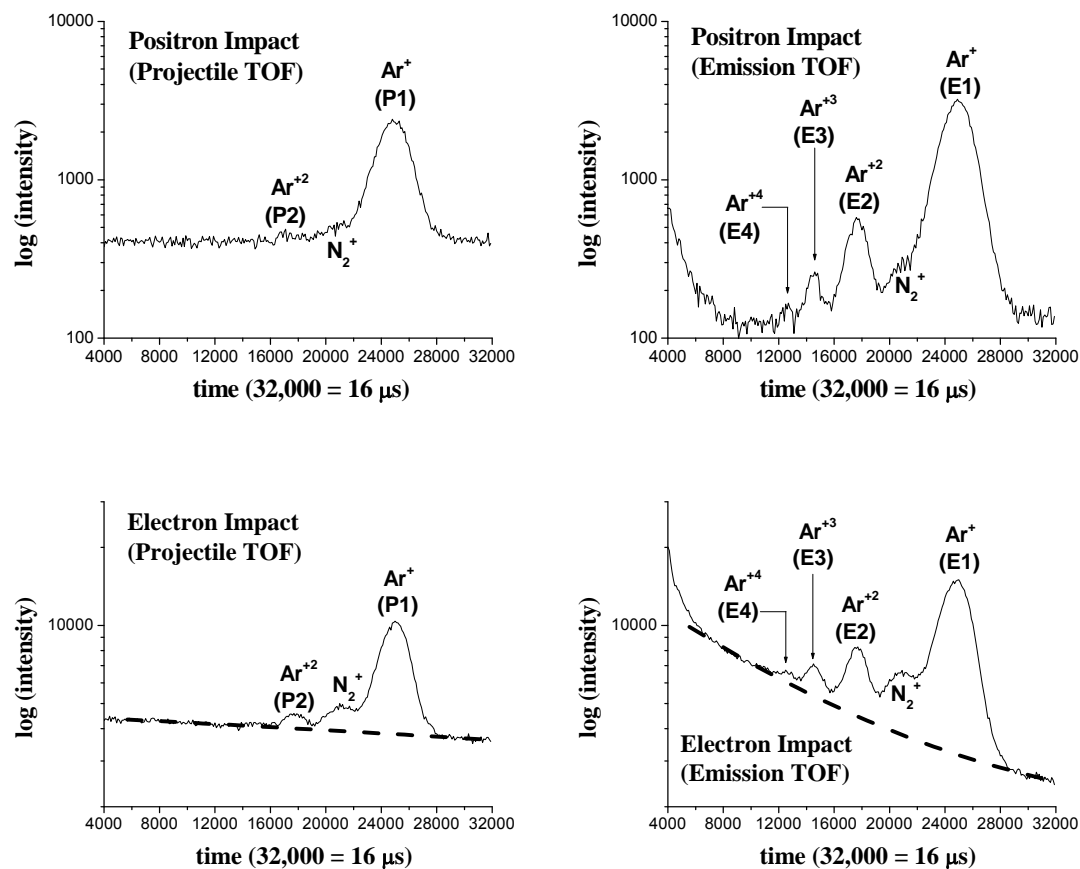
Figure 3.1.   Times of Flight.

This figure contains times of flight spectra for projectile-ion coincidences (left figures) and for emitted electron-ion coincidences (right figures). Thin solid lines represent coincidences and thick dashed lines represent a background fit. Peaks for single and multiple ionization are shown.

When corrected for detection efficiencies, etc., the peak areas determine the relative

probabilities between different degrees of ionization. However, the probabilities are not

total probabilities since not all of the collision partners, e.g., projectiles or electrons, are

detected due to energy and angular measurement limitations. To obtain the peak areas, a

background subtraction for the scattered projectile and electron emission channels is

performed in which the "random" events are removed.   For the sake of clarity, the words

"background" and "coincidences" will be used in reference to "random" and "real"

events, respectively. To obtain background subtracted spectra during the Cobold sorting

procedure, a "pure background" 2D spectrum was created by using a background window

located close to the peak of interest and whose area was scaled with respect to the TOF

peak of interest (Fig. 3.2, Fig. 3.3). The background is scaled according to a

mathematical fit when the background is not constant (Fig. 3.1). Statistical errors for this

procedure were calculated from the resulting background using the following formula.

All proceeding data presented are background subtracted in this manner.

$$e = \text{events}; \text{bg} = \text{background} \tag{2}$$

$$\text{SE} \equiv \pm\left[(e - \text{bg}) - \left((e - \sqrt{e}) - (\text{bg} + \sqrt{\text{bg}})\right)\right] = \pm\left[\left((e + \sqrt{e}) - (\text{bg} - \sqrt{\text{bg}})\right) - (e - \text{bg})\right]$$
$$= \sqrt{e} + \sqrt{\text{bg}} \tag{3}$$

In reference to Figure 3.1 above, the coincidence peaks have been identified as

mentioned in Section 2.8 above. Upon comparison, a difference between positron and

electron impact can be seen regarding the relative magnitude of double ionization peak,

Ar^{+2}, to the single ionization peak, Ar^+, in the projectile time of flight. This is attributed

to the lower double ionization cross section for positron impact discussed in Section 1.3.1

above. Higher degrees of ionization are also detected in the emitted electron TOF since

this detector is much closer to the interaction region where larger angles are observable in

contrast to the projectile detector, which also has an upper limit on detectable energy loss

and scattering angle required for multiple ionization. Raw statistics have been extracted

from the TOF spectra and presented in Table 3.1 below.

In Table 3.1, the total numbers of coincidences excluding background are listed

for each coincidence type and for both electron and positron impact. The corresponding

Table 3.1.   Raw statistics.

Coincidence Type	Electron Impact	Positron Impact
	Real only (bg only)	Real only (bg only)
projectile-Ar$^+$ (**P1**)	197,402 (125,614)	50,998 (27,190)
projectile-Ar^{++} (**P2**)	13,143 (110,446)	945 (9,037)
emission-Ar$^+$ (**E1**)	179,223 (52,740)	52,630 (5545)
emission-Ar^{++} (**E2**)	29,306 (37,720)	3,751 (2,390)
emission-Ar^{+++} (**E3**)	6,157 (40,195)	547 (1593)
projectile-Ar$^+$ - emission (**P1E1 or E1P1**)	36,984 (11,073)	10,903 (123)
projectile-Ar^{++} - emission (**P2E2 or E2P2**)	4,885 (9,474)	260 (20)

background is given adjacent to the totals in parenthesis. Also, the different coincidence types are given abbreviations. The P1E1 and E1P1 abbreviations refer to the same type of coincidence, though P1E1 refers to coincidences viewed by the projectile PSD and E1P1 refers to coincidences viewed by the emission PSD. The same designation applies to P2E2 and E2P2 coincidences.

3.1.2.   2D Spectra. Two-dimensional (2D) spectra are also created for single and multiple ionization plus appropriate backgrounds for both the scattered projectile and ejected electron channels. The 2D projectile spectra provide information about the post-collision scattering angles (Fig. 3.3) and projectile energies (Fig. 3.4). Vertical or horizontal slices (projections) of the 2D spectra are used to generate one-dimensional (1D) spectra in order to highlight particular aspects of the data. For example, the projectile energy loss for a particular range of scattering angles or the scattering for

certain energy losses can be generated using horizontal and vertical slices of data as demonstrated in Figure 3.2. The data used in Figures 3.2 – 3.6 are from positron impact and identical procedures are used for the generation of 2D electron impact spectra. From the projectile TOF in Figure 3.2, two 2D spectra are generated using the events indicated by the shaded areas. The lighter and darker shaded areas between the dotted lines represent background and coincidences, respectively. The shading in the 2D spectra is an indication of event intensity. As shown, the background (BG) spectrum is subtracted from the ionization peak (P1 + BG) spectrum leaving a spectrum (P1) containing only real coincidences. The majority of the 2D background spectra can be attributed to the beam and thus establishes the location of the beam.
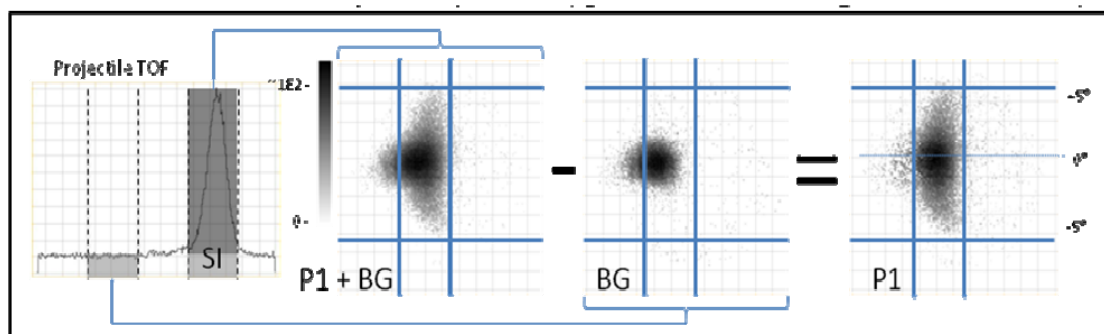
Figure 3.2. 2D Projectile Spectrum Generation.

This figure illustrates the background subtraction and generation of a 2D projectile spectrum. The lines isolate coincidences into 1D projections.

From the 2D spectra, 1D, vertical projections (Fig. 3.3) of the areas between the vertical thick solid lines (Fig. 3.2) show the scattering angles for a specific energy range. The background projections are used to calculate statistical error bars for the 1D coincidence spectrum (P1). The background peak intensity defines the zero degree

scattering center. As for this energy range, zero scattering is shown to dominate with a

reduction in intensity as the scattering angle increases.
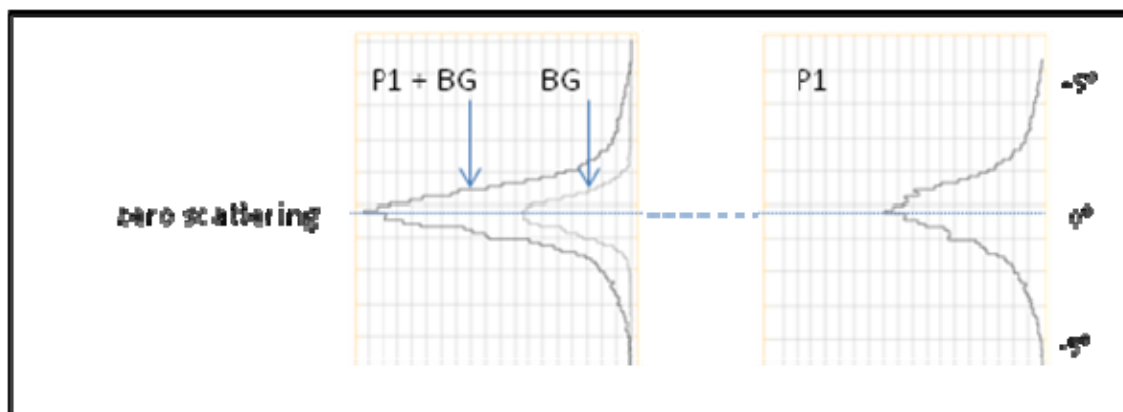
Figure 3.3.   Scattering Angle Projections.

This is an illustration of a vertical projection of the 2D projectile spectrum showing the real plus
random intensity (P1+BG), the random background intensity (BG), and the difference (P1).

The 1D, horizontal projections (Fig. 3.4) show the energy losses for the scattering

angles between the thick horizontal lines in the 2D spectra (Fig. 3.2). The thin blue line

labeled "15 eV" is a physical representation of the ionization potential of Ar, which is

actually 15.76 eV. Coincidences in the P1 distribution represent projectiles that have lost

at least the IP energy and scattered in the specified angular range. These projectiles

originated from within the horizontal beam limits and were displaced to the right by at

least the minimum distance represented by the IP. Due to poor energy resolution, there is

overlap between the non-interacting beam (BG) and the ionization peak (P1).
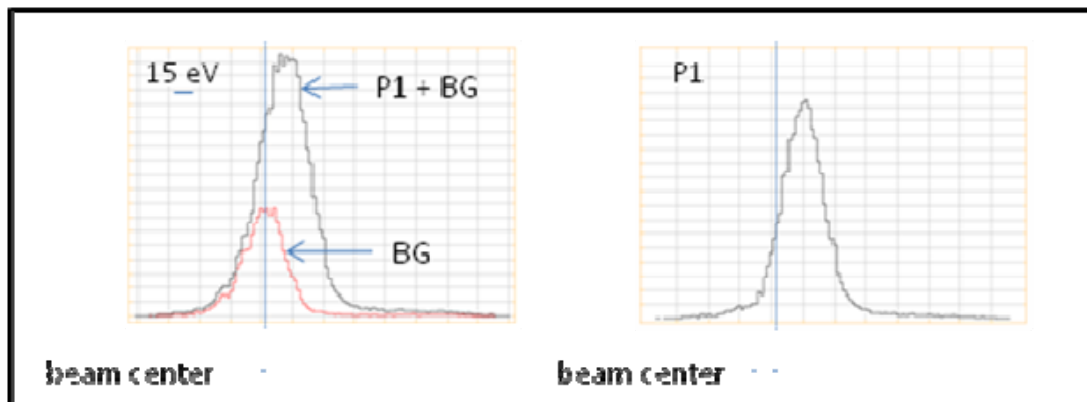
Figure 3.4.   Energy Projections.

This is an illustration of a vertical projection of the 2D projectile spectrum. On the right, the small red peak is the background (BG) and represents the beam which hasn't suffered any energy loss. The IP is represented by the horizontal blue line labeled "15 eV." The large peak (P1+BG) represents ionization plus background and the overlap between the BG and P1+BG peak is due to poor energy resolution. The background free projection (P1) is shown on the left and is displaced to the right of the beam center due to energy loss.

The 2D electron emission spectra contain information about the electron emission angles (Fig. 3.5). Similarly, the forward or backward electron emission with respect to the beam direction can be generated from the electron 2D spectra by taking a horizontal slice as demonstrated in Figures 3.5 - 3.6. For the emission TOF (Fig. 3.5), the same procedure used in Figure 3.2 is applied here for the creation of a 2D background free, emission spectrum (P1). Forward emission coincides with the forward direction of the beam orientation indicated by the thick arrow.

Projections (Fig. 3.6) of the 2D spectra parallel and symmetric to the beam orientation show straight trajectory emission angles from 35 to 155° with respect to the interaction region located in the center of the spectra. The emission origin is located in the center of the projection. Therefore, these projections qualitatively show more forward scattering than backward scattering.
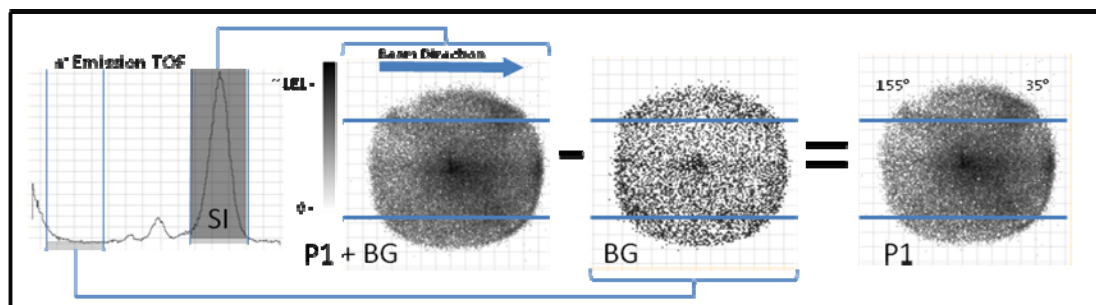
Figure 3.5. 2D Emission Spectra Generation.

This is an illustration of how a 2D emission spectra is generated, background subtracted, and projected into a 1D spectrum. P1+BG is the emission 2D spectrum sorted for only events inside the SI TOF window. BG is the emission 2D spectrum sorted for only events inside the background window. P1 is the difference.
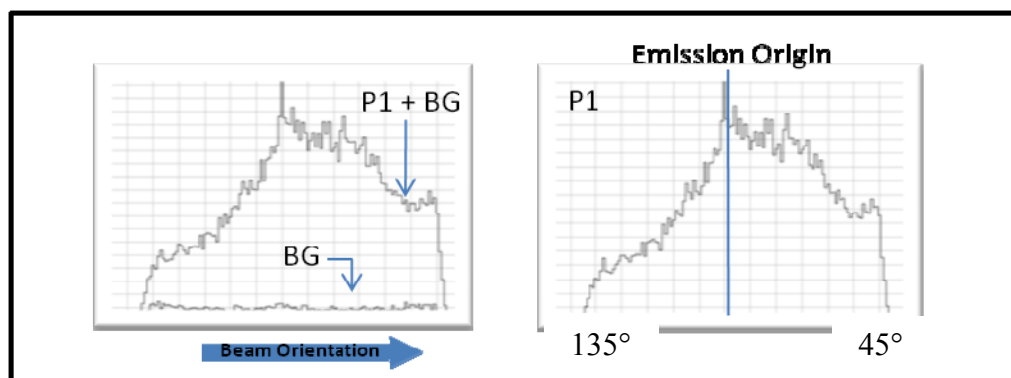
Figure 3.6. Emission Projections.

An illustration of 1D projections of the 2D emission spectrum for the three cases in Fig. 3.5.

3.1.3. Triple Coincidences. Triple coincidences, designated by E1P1 or P1E1 with the first letter designating the particle being observed and the second letter the coincidence partner, are generated by combining conditions from the scattered projectile and the electron emission TOF. For example, the projectile (electron) single ionization 2D spectra are restricted to events where the emitted electron (scattered projectile) is also detected by setting an additional window on electron (projectile) single ionization TOF

peak (Fig. 3.7). The background is generated in the same manner except that these events are restricted to a pure background region of the TOF spectra.

Once the P1E1 and E1P1 spectra are generated, there is a one-to-one correspondence between the scattered projectiles and emitted electrons, and therefore, all kinematic information regarding the ionization interaction is known. These triple coincidences can be restricted further by applying spatial conditions with respect to either 2D spectrum specifying energy loss and scattering angle (horizontal and vertical conditions on the P1E1 2D spectra), or forward or backward emission (horizontal conditions on the E1P1 2D spectra).

3.1.4.   Raw Angular and Energy Distributions. The total number (after background subtraction) of each type of projectile coincidence is given in Table 3.1, along with the respective background in parenthesis. In Figure 3.8, angular distributions obtained using restrictions as described above are displayed for the various projectile coincidence spectra. The plots include both positron (empty circles) and electron (solid squares) data. For the sake of clarity, negative error bars extending to zero have been omitted.

These projectile scattering curves illustrate how double ionization leads to larger scattering angles plus (not easily observable in the displays shown) how adding a coincidence with the detected electron enhances the "negative" projectile scattering, i.e., binary interactions.

Total projections (all coincidences) of all projectile coincidence types are shown. Electrons (positrons) are represented by solid squares (open circles). The beam center is at channel -20 (energy) and channel 0 (scattering). Also, recall that FWHM is 14 and 12

channels for electron and positron impact, respectively. These plots are meant to give the

reader a feel for the statistics and error bars.
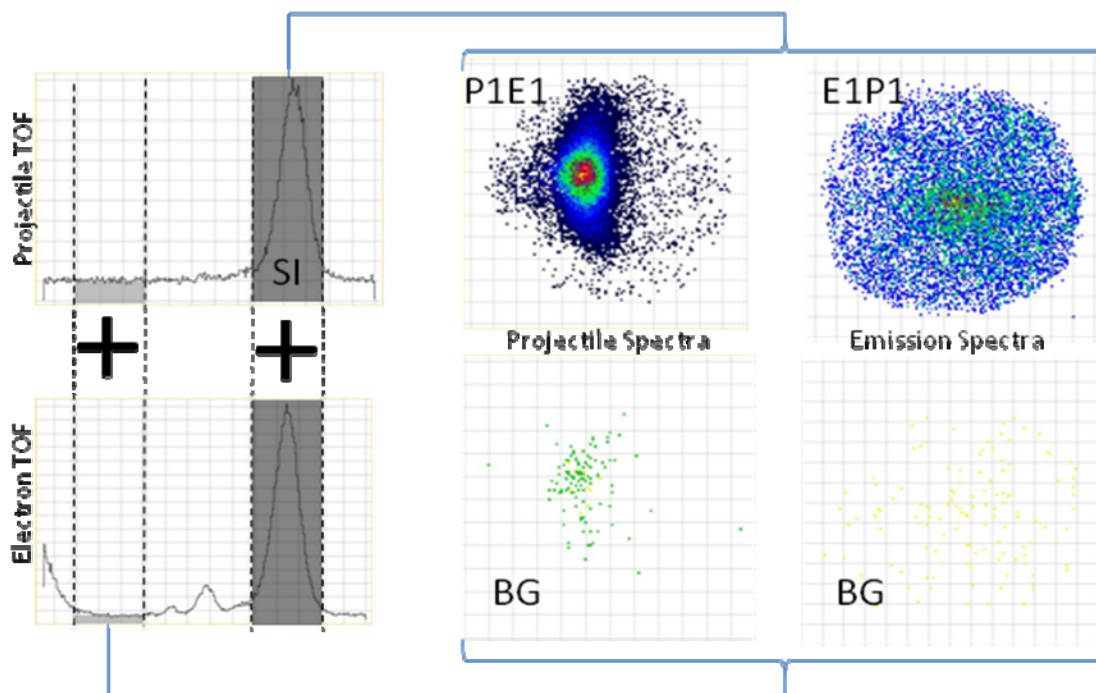
Figure 3.7.   Triple Coincidence Events.

This is an illustration of how a triple coincidence is established. Only coincidences that are mutually inclusive in the single ionization peaks (or in the random regions) of both the emitted electron and projectile TOF are included in the P1E1 (BG) and E1P1 (BG) spectra. The upper 2D figures show the signal plus backgrounds in the projectile and emission channels while the lower 2D figures show only the background contributions.
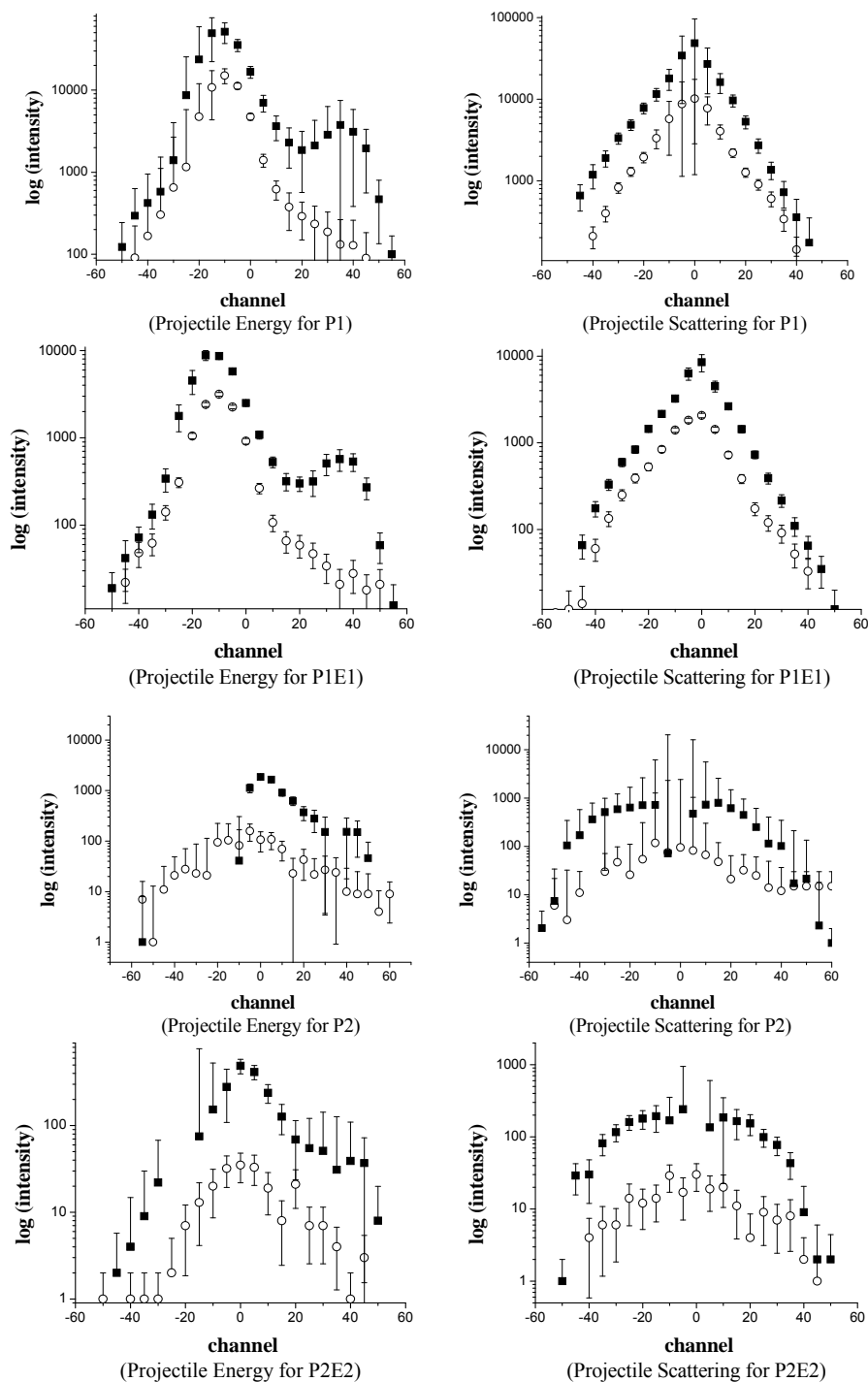
Figure 3.8.   Projectile Energy Loss and Scattering Comparisons.

Non-convoluted energy (horizontal) and non-calibrated scattering (vertical) 1D projections for single (upper 4 figures) and double (lower 4 figures) ionization. Solid squares; electron impact. Empty circles; positron impact. The left figures show one-dimensional projections along the energy axis thus providing energy loss information. The right figures show projections along the scattering angle axis.

3.2.   ENERGY CALIBRATION

3.2.1.   Beam Image Width.   To calibrate the energy (horizontal) axis in the projectile 2D spectra, various energy electron or positron beams were produced and imaged on the detector (Fig. 3.9).   Then the positions of the maximum intensity were plotted versus the beam energy and fitted to a line.   This gave the eV/horizontal channel calibration with the absolute scale during a coincidence measurement being determined from the maximum location of the beam intensity observed in the projectile 2D background spectrum being set to the beam energy.
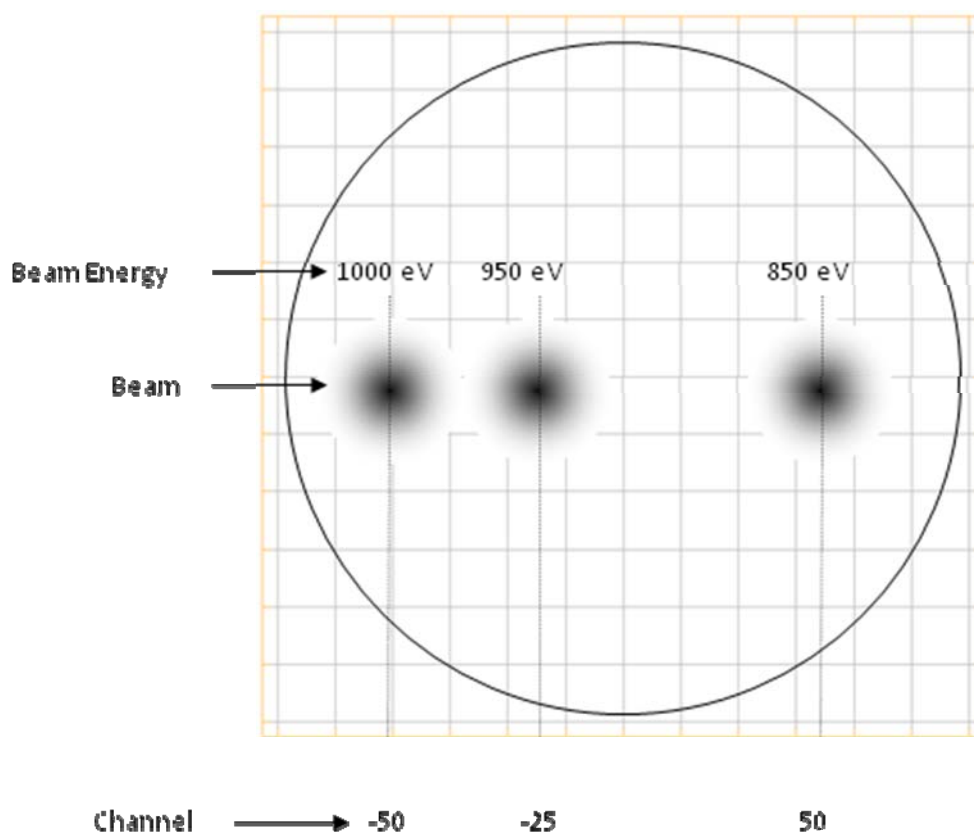
Figure 3.9.   Energy Calibration.

This is an illustration of how the projectile spectrum is calibrated for energy (horizontal).   The beam energy is incrementally lowered creating the images shown.

In this example, each 50 eV change in the beam energy results in a shift of the maximum beam intensity by 25 channels. Therefore the energy calibration is 2 eV/channel in the example. Using this method, the 1keV data presented was calibrated to be 4 eV/channel.

3.2.2. Energy Loss Convolution. While this determination of the energy calibration per channel was a straight forward procedure, the energy loss calibration is complicated by the broad horizontal width of the beam image. According to SIMION modeling, the spectrometer should focus identical energy projectiles to the same horizontal channel. Our modeling also confirmed that a 3 eV [65] width of the energy distribution of the moderated positrons does not account for the image width that we observe. Therefore, the image width is attributed to physical beam width rather than a wider energy distribution. Beam dispersion, the interaction chamber entrance aperture, and the vertical entrance slit width of the spectrometer are the determinants of the physical beam width. This means that although a Gaussian horizontal beam profile is observed, this profile represents differences in beam intensity rather than differences in beam energy, i.e. all horizontal channels in this profile correspond to the full beam energy (including of course the initial energy spread from the source). The horizontal full width at half maximum intensity (FWHM) of the electron and positron beam is 14 and 12 channels, respectively.

This finite beam width introduces uncertainty in the projectile energy loss of each projectile-recoil ion coincidence channel, i.e., at a "specific" energy loss channel, we must account for the fact that to end up at the same energy loss channel the far side of the beam has suffered a larger energy loss than the near side of the beam. In order to

determine what energy losses contribute at a particular coincidence channel and how much of the observed signal is associated with each energy loss, the following procedure was used. The procedure is simply a way of correlating coincidences to the contributing beam intensities. First, we note that the single ionization potential of Ar is 15.76 eV. This poses the requirement that a projectile must transfer at least 15.76 eV to an Ar 2p valence electron before a single ionization can occur, which means that ionization associated with the left side of the Gaussian beam profile will be detected at 15.76 / 4 channels to the right whereas ionization associated with the central and right side of the profile will occur some channels later. In other words, if the only energy loss was 16 eV, then the ionization events would also have a Gaussian profile but shifted to the right by 4 channels. Thus, coincidences within a particular vertical channel of a 2D spectrum correspond to emission energies given by (4eV/channel) * X - 15.76eV where X is the displacement between the various channels of the beam image and the coincidence channel. Since the beam image has finite width, this means that there is a range of possible energy losses for a particular channel. However, near the onset of ionization, the right hand portion of the beam image cannot contribute to the energy loss in channels closer than 15.76 eV or 15.76 / 4 channels. Furthermore, the contribution of each energy loss to the coincidence signals in channels within this range is proportional to the intensity of the beam image corresponding to that particular energy loss. In other words, starting at the farthest "highest energy" part of the beam profile one determines the relative amount of the total beam intensity and multiplies this by the energy loss determined from the number of channels this point is away from the ionization signal of interest. This procedure is then repeated for the next closest portion of the beam profile,

etc. until the entire beam profile has been included or the energy loss becomes less than the ionization potential. At that point, the average energy loss (plus the range of energy losses) is calculated by dividing by the entire beam profile intensity.

3.2.3. Gaussian Fit. In practice, we represented the beam image by a Gaussian distribution and determined the average and range of energy losses contributing to each coincidence channel. The Gaussian, normalized to 1, is given by

$$y = y_0 + \exp\left(\frac{-2 \cdot (x - x_0)^2}{w^2} \right) \tag{4}$$

where y_0 is the baseline offset, x_0 is the location of the maximum, and $w/2$ is the standard deviation which is approximately 0.425 the width of the peak at half height (FWHM).

Origin was used to fit a Gaussian function to the beam image using a nonlinear regression method. Origin's nonlinear regression method is based on the Levenberg - Marquardt algorithm and is the most widely used algorithm in nonlinear least squares fitting. In cases where a portion of the beam image was restricted from contributing because the energy loss was less than the ionization potential, the beam intensity was renormalized. A FORTRAN program was created to perform the Convolution.

3.3. PROJECTILE ENERGY LOSS AND SCATTERING

3.3.1. Convoluted Energy Loss. Projectile energy losses up to 300 eV could be detected for the spectrometer settings used during data collection. Convolution results for some of the projectile coincidence data are shown in Figure 3.10. The data presented was obtained from a limited region of the projectile spectrum such that detector edge uncertainties with respect to any portion of the beam which could hit and scatter from the detector mounting plate or restrictions due to the circular detector shape would not

influence the data. The scattering limits were ±5° for all projectile coincidences.

Although on axis, the total width of the projectile spectrum spanned 110 channels, the

projectile single and double ionization coincidence energies (x channels) were limited to

regions 30 and 55 channels wide, respectively. The counts excluded from the P1

coincidences, i.e., outside the 30 channel wide region, contributed less than 1%.
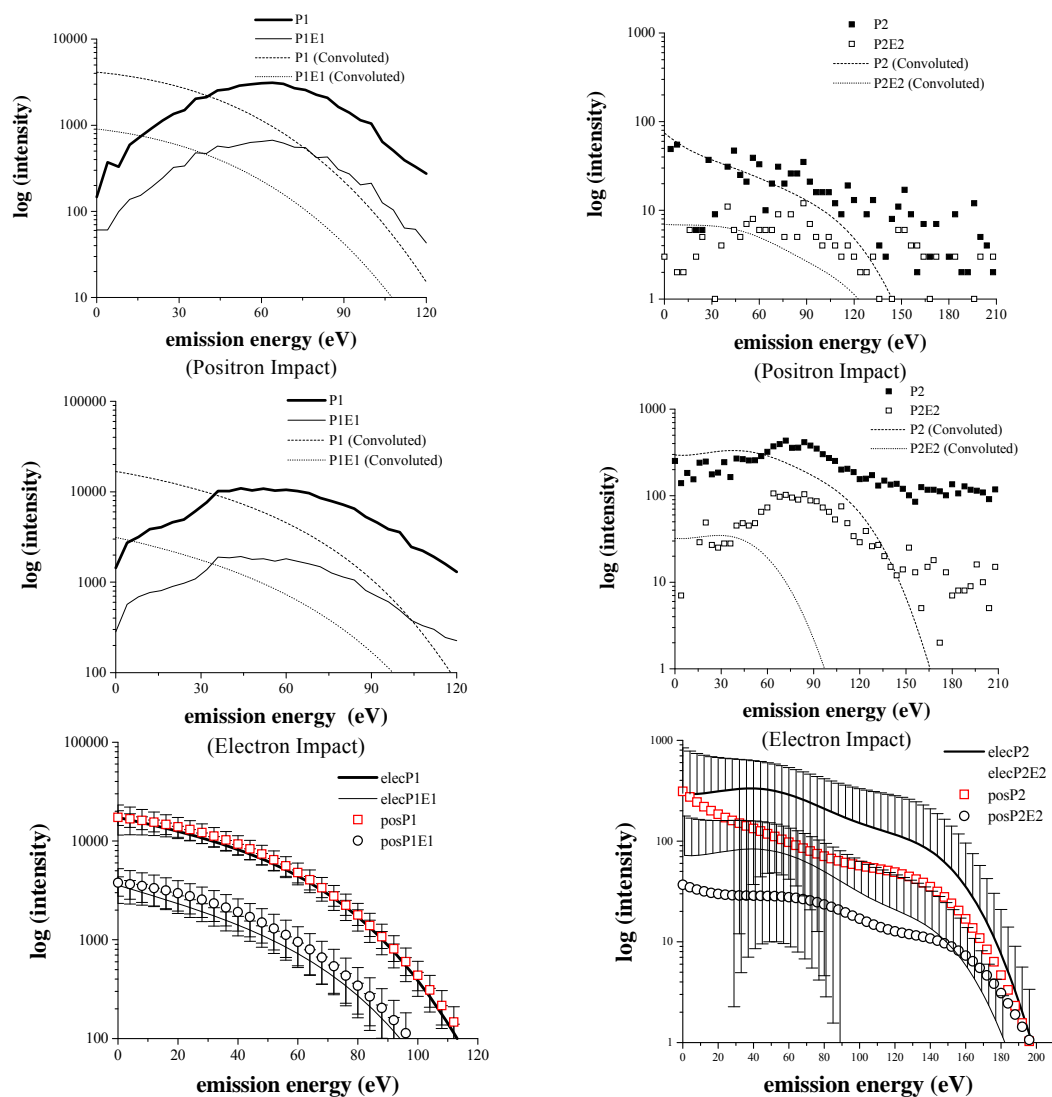

Figure 3.10.   EnergyConvolutions.

This figure compares non-convoluted to convoluted emission energy. First row; positron impact.
Second row; electron impact. Third row; comparisons of the convolutions. In the top 4 plots, the
convolutions are labeled in the legend. In the bottom row, the plots contain only the
convolutions.

In the first four plots of Figure 3.10, there are non-convoluted and convoluted energy distributions. Adding the IP to the emission energy will produce the projectile energy loss. The non-convoluted distributions are put on an energy scale by using the displacement (incorrect energy) calibration (4eV/channel) between the ionization channel and the beam center. The convoluted distributions, in contrast, show a sharp onset of ionization followed by a decline in intensity. This difference arises from the uncertainty of the energy loss of the ionization channel due to the beam width. This uncertainty is converted into a Gaussian distribution (beam profile) as discussed above.

3.3.2. Energy Loss at Various Scattering Angles. Figure 3.11 shows the projectile energy loss distributions for different scattering angles. To illustrate the kinematic effects, raw (non-convoluted energies) data are used. Due to conservation of momentum and energy, the projectile scattering angles increase as the emission energy increases. This is evident in Figure 3.11 where the 2D spectra of the P1 and P1E1 coincidences for electron and positron impact were divided symmetrically among four different scattering angle ranges and projected horizontally into the 1D distributions. The two center distributions in each plot represent angles of $0.5° \pm 0.5°$ for upward and downward scattering (denoted by positive and negative angles, respectively). Remember that for the triple coincidence measurements, the electron detector is above the beam axis. From top to bottom (Fig. 3.11), the distributions represent scattering angles of $4° \pm 1°$, $2.5° \pm 0.5°$, $1.5° \pm 0.5°$, $0.5° \pm 0.5°$, $-0.5° \pm 0.5°$, $-1.5° \pm 0.5°$, $-2.5° \pm 0.5°$, and $-4° \pm 1°$. In generating these data, the final bin size was doubled to improve the statistics. Error bars for the overall statistics can be found above in Figure 3.8.
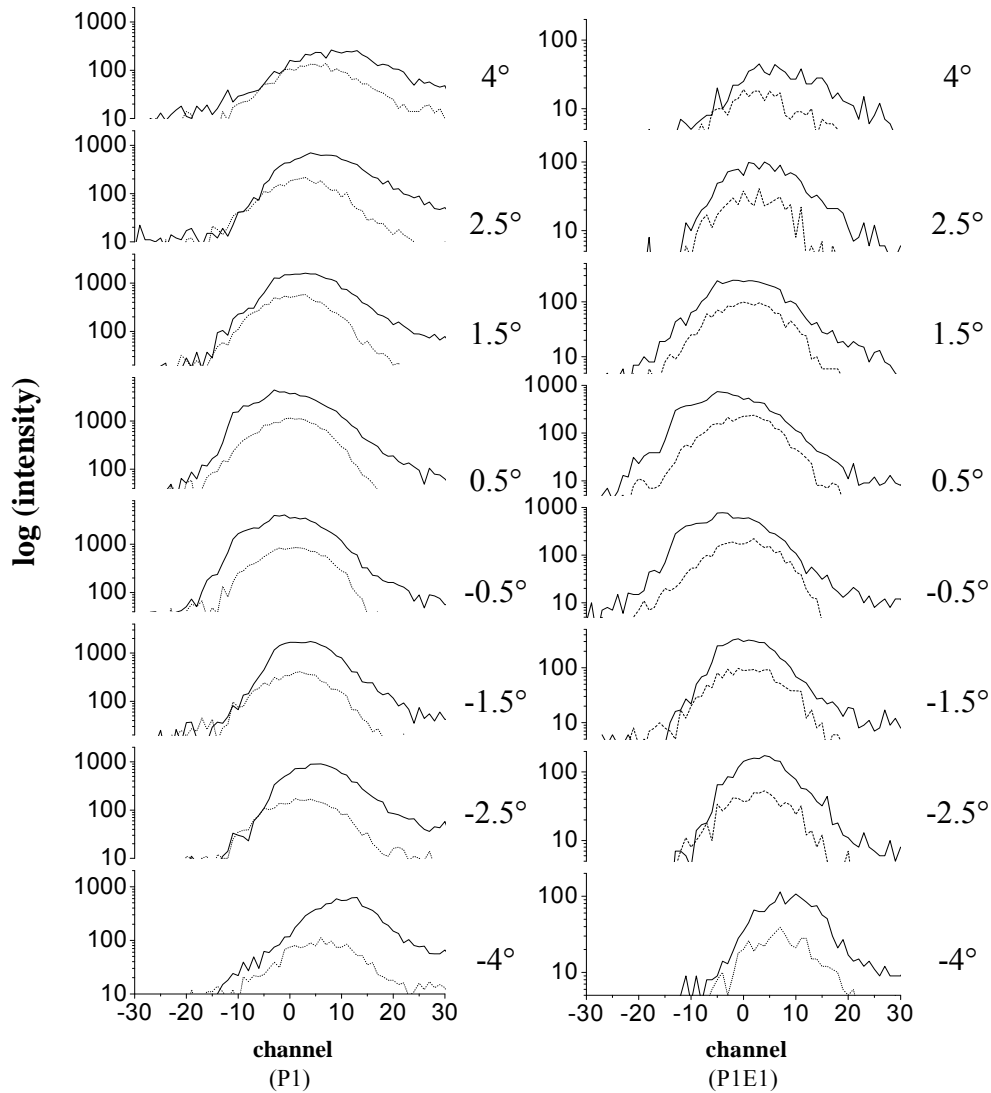
Figure 3.11. Single Ionization Energy Distributions.

Non-convoluted (raw) energy loss of various scattering ranges. The left plot presents P1 data and the right plot presents P1E1 data. Electron (positron) impact data are represented by a solid (dotted) line. FWHM is 12 (positrons) and 14 (electrons) channels centered at channel -10. Profiles symmetric about zero scattering are placed on the same vertical log scale for comparison.

Both projectiles show a shift to higher energy loss as the scattering angle

increases, which is simply a consequence of the conservation of momentum. Though

both projectiles show similar overall energy dependencies, electron impact displays a

larger energy shift from smaller to larger scattering angles. Both projectiles show larger binary (scatter down) intensities as shown in the P1E1 energy distributions.

3.3.3.   Projectile Scattering. The projectile scattering was investigated by comparing the P1E1 and P1 spectra at different energy losses. With regard to projectile scattering, there is an important difference that exists between P1 (doubly differential) and P1E1 (triply differential) coincidences. During P1 interactions, there is symmetric scattering with respect to the beam axis. However, if the scattering is measured in coincidence with the emitted electron, the symmetry is broken and two types of interactions, named binary and recoil, can be distinguished. Since the position of the emitted electron detector is above the scattering center, the indication of a binary interactions is when a projectile scatters down and is in coincidence with an upward emitted electron i.e., P1E1 coincidences for negative scattering angles. Vice versa, the upward scattering P1E1 coincidences indicate recoil interactions, i.e., where the projectile scatters upwards and the electron is emitted in a downward direction but is turned around by the nucleus and ends up being detected in the upward direction. This reasoning provides a method of mapping the electron emission in which all kinematical information is known as will be done in the next section.

Figure 3.12 shows the projectile scattering for emission energies of 12, 17, 25, 36, 50 and 70 eV. Each distribution was obtained by projecting 10 channels wide vertical slices of the background subtracted spectrum with each successive slice overlapping the previous slice by 5 channels. To remove any experimentally introduced scattering non-symmetry for downward (corresponding to binary collisions in the P1E1 spectra) and upward (corresponding to recoil collisions in the P1E1 spectra) scattering ratios of P1E1

to P1 coincidences were calculated for each energy loss. These ratios were taken for positron (empty circles) and electron (full squares) impact and are shown in Figure 3.12. The P1E1/P1 ratios show that electron impact results in relatively isotropic projectile scattering compared to a positron ratio that displays a higher binary (downward) scattering yield. This implies roughly equal probabilities for binary and recoil interactions for electron impact in contrast to more binary interactions for positron impact.
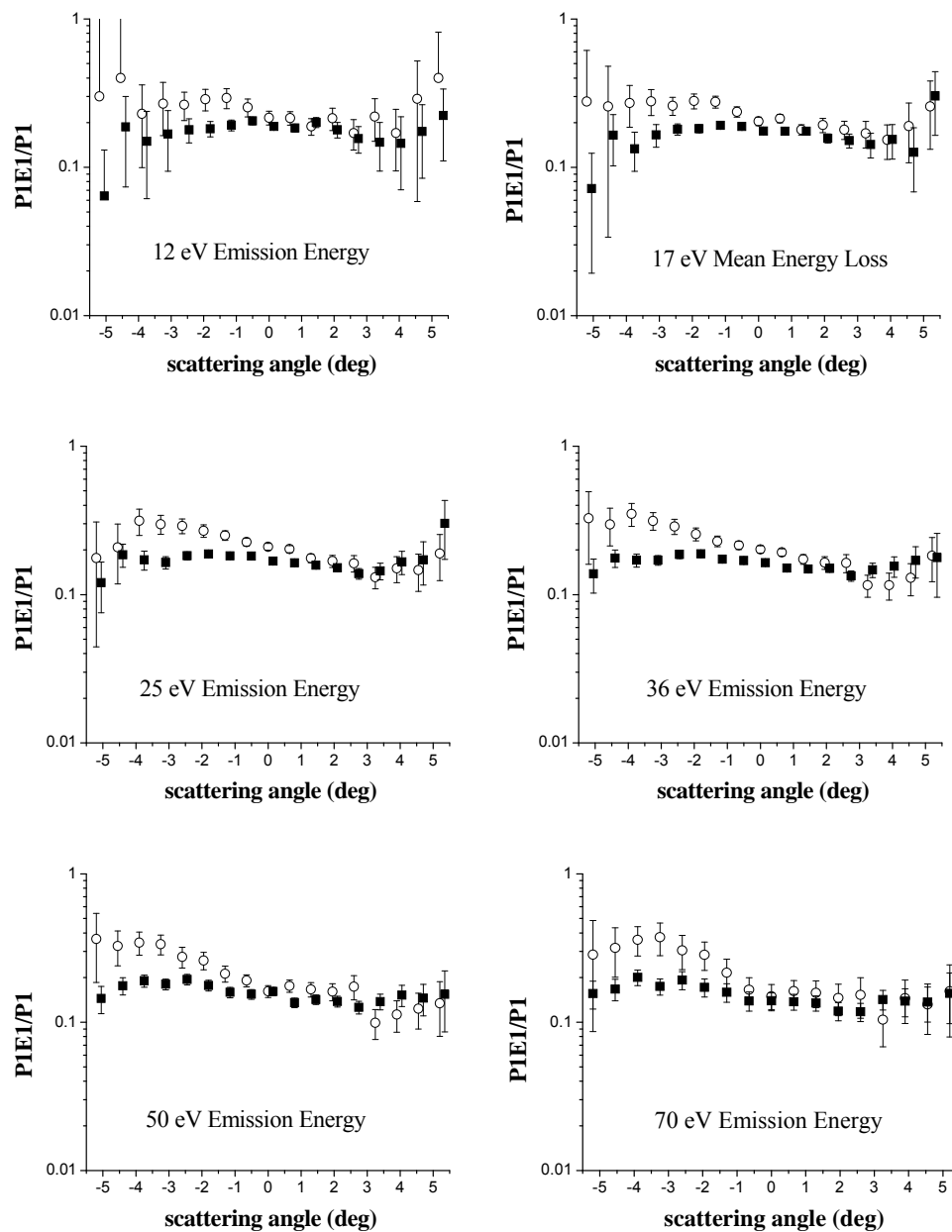
Figure 3.12.   Projectile P1E1 to P1 Scattering Ratios.

This figure compares the ratios of P1E1 (broken symmetry) over P1 (symmetric) for various emission energies with respect to projectile scattering angle. Positron impact; empty circles. Electron impact; solid squares.

3.4.   TRIPLY DIFFERENTIAL ELECTRON EMISSION

The E1P1 spectrum in combination with the P1E1 spectrum provides all

kinematic (triply differential) information of single ionization events occurring within the

experimental limitations. The traditional method of displaying TDCS is to plot angular

distributions of the emitted electron-scattered projectile coincidence intensity as a

function of the emission angle, for selected electron energies and projectile scattering

angles. To generate these data the following procedure was used. The first step is to

generate 2D projectile spectra using conditions where single ionization has occurred and

a scattered projectile and emitted electron are both detected, i.e., foreground P1E1

spectra. Next 2D background spectra are generated for conditions where a) random

coincidences are recorded in, both, the scattered projectile and emitted electron channels

plus b) a random coincidence occurs in either of the channels simultaneous with a real

single ionization in the other channel, i.e., background P1E1 spectra. Then in the

foreground and the background P1E1 2D spectra, conditions are placed on a specific

range of energy loss and of scattering angles symmetric about 0°. This is illustrated in

Figure 3.13 by the white and black boxes in the P1E1 foreground and BG spectra.

Using these energy losses and scattering angles the electron emission spectra are

sorted. This results in the generation of 2D E1P1 foreground and BG spectra for scatter

up (positive scattering angles) and scatter down (negative scattering angles) projectiles.

After background (BG) is subtraction, projections are taken along the beam direction.   In

principle, for a narrow entrance slit to the projectile spectrometer and larger scattering

angles, the collision plane is well defined; in practice to obtain enough statistics for

positron impact small scattering angles and a wider entrance aperture were required. This

means that the collision plane is less well defined, especially for the smallest scattering

angles. Also, and again to improve the statistics, a relatively wide slice along the beam direction was used, namely $\varphi_e \leq \pm 32°$. These 1D projection spectra represent TD emission for recoil (scatter up) and binary (scatter down) interactions for a specific momentum transfer. Again, in order to improve statistics, the projections are binned by 5 channels and are shown in polar plots.
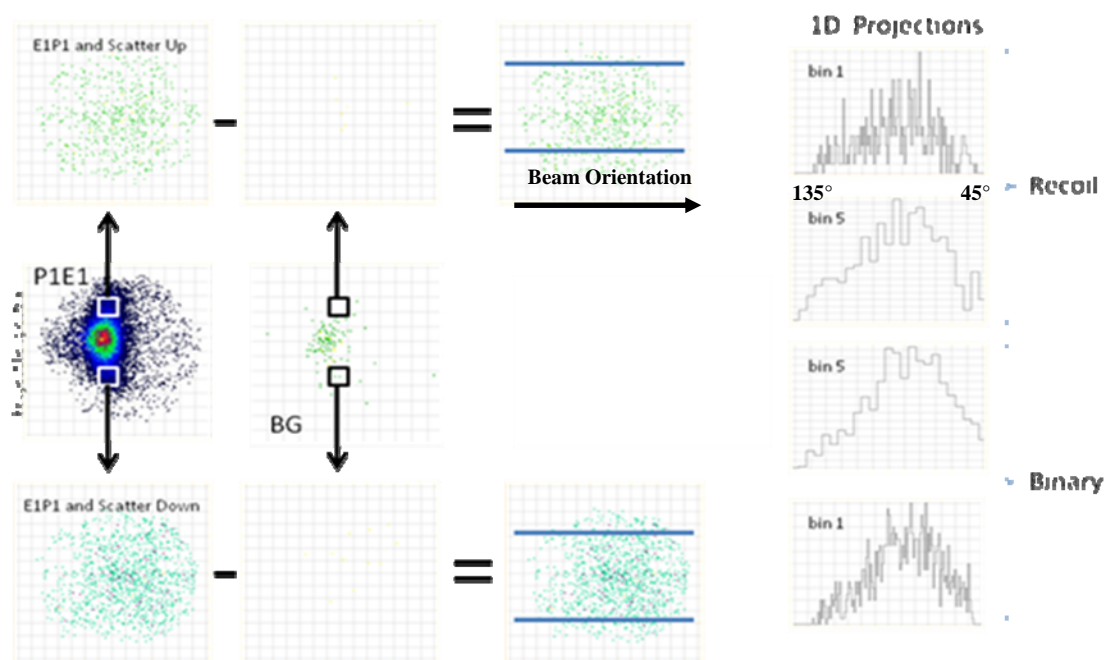
Figure 3.13. Triply Differential Emission Generation.

This figure illustrates how the binary and recoil distributions are generated. On the left, the boxes show symmetric regions about zero scattering which establish the energy loss and scattering angles of the projectile. Using these for signal plus background (far left 2D spectrum) and background only (second from left 2D spectrum), the 2D electron spectra are sorted and the background is subtracted. Slices along the beam direction are taken (middle 2D spectra) and 1D projections of the electron emission are obtained (far right 1D spectra). Emission spectra generated from a projectile scatter up (scatter down) region show recoil (binary) emission.

The method for analyzing the TD data also involved creating a FORTRAN program which simulates the experimental conditions in order to convolute "ideal" momentum transfer lobes to experimental conditions for comparing with the measured

data. Most importantly, the program simulates the ion extraction field and solid angle

plus grid transmission effects. Additionally, the program calculates the direction and

magnitude of the binary and recoil lobes and emission energy using information obtained

from the P1E1 spectrum. Other adjustable parameters integrated into the simulation

include the widths of the binary and recoil lobes, the scattering center position, target

intensities with respect to the scattering region, beam diameter and intensity profile, post

collision shift of the binary lobe due to the scattered projectile, and an additive constant

to the input lobes. The target and beam intensities are modeled by cosine distributions.

The momentum transfer lobes are modeled by a cosine-squared distribution. In the

following figures this modeling shows how the intensities at the forward and backward

angles are reduced due to grid transmission and solid angle effects. The electric field

influences lower emission energies. The combination of the effects influences the

observed maximum intensity with respect to the momentum transfer direction.

In the following figures (Fig. 3.14 – 3.18), emission data from two different

energy ranges and three different scattering ranges are presented along with the emission

energy distributions and a comparison of the emission to a convolution of cosine squared

momentum transfer lobes with a mean energy equal to the mean energy of the observed

emission. Therefore, there are six plots of emission data and they are referred to as, for

example, emission 1-2 such that the first number, 1 in this case, identifies the energy

range and the second number, 2, identifies the scattering range, i.e., the horizontal and

vertical ranges selected. Energy range 1 has a mean ejected electron energy of 21 eV

(positron impact) and 22 eV (electron impact). Energy range 2 (Fig. 3.20) has a mean

energy of 39 eV (positron impact) and 46 eV (electron impact). Fig. 3.14 shows how

specific energies contribute within range 1 and range 2. High energy ranges were chosen

so that extraction field effects would be minimized. The mean scattering angles are 1.2,

2.1, and 2.9° for scattering ranges 1, 2, and 3, respectively.
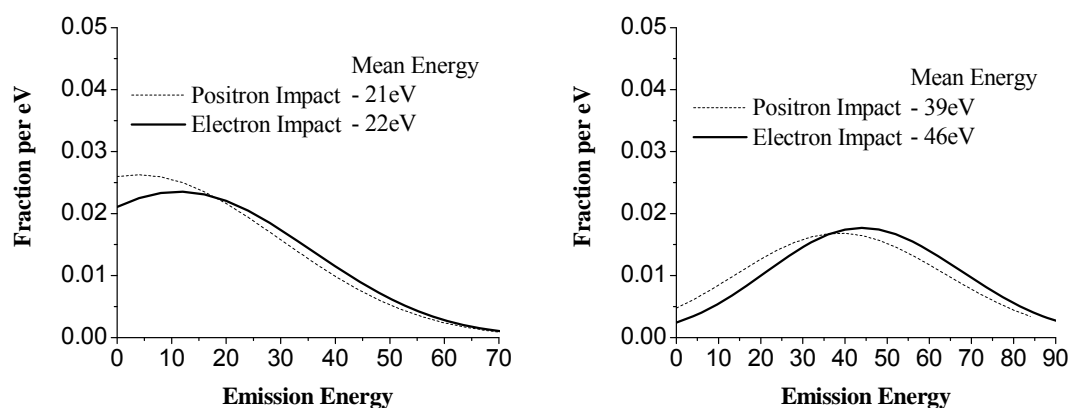
Figure 3.14.   TDCS Energy Ranges 1 and 2.

This figure compares the emission energies plus the relative contribution of each energy for
positron and electron impact which contribute to energy range (left) 1 and 2 (right).

Figure 3.15 shows the input momentum transfer lobes that were convoluted with

the experimental conditions in order to be directly compared to measured emission data.

The lobes are labeled bindn, recdn, binup, and recup where bin and rec refer to binary

and recoil, and the suffixes dn and up refer to down and up according to the projectile

scattering. In Figure 3.15, the projectile has scattering down (the horizontal arrow

emerging from the center) and the electron emission detector would be located above the

polar plot. Thus, the black and red lobes correspond to binary and recoil electrons,

respectively, for this downward scattered projectile. For upward scattered projectiles (not

shown), the green and blue lobes represent binary and recoil electron emission. With the

location of the electron detector, the black lobe illustrates the emitted electron-downward scattered projectile coincidences and the blue curve illustrates the emitted electron-upward scattered projectile coincidences. These lobes have the same mean energy and mean scattering angle as the emission presented in Figure 3.17.
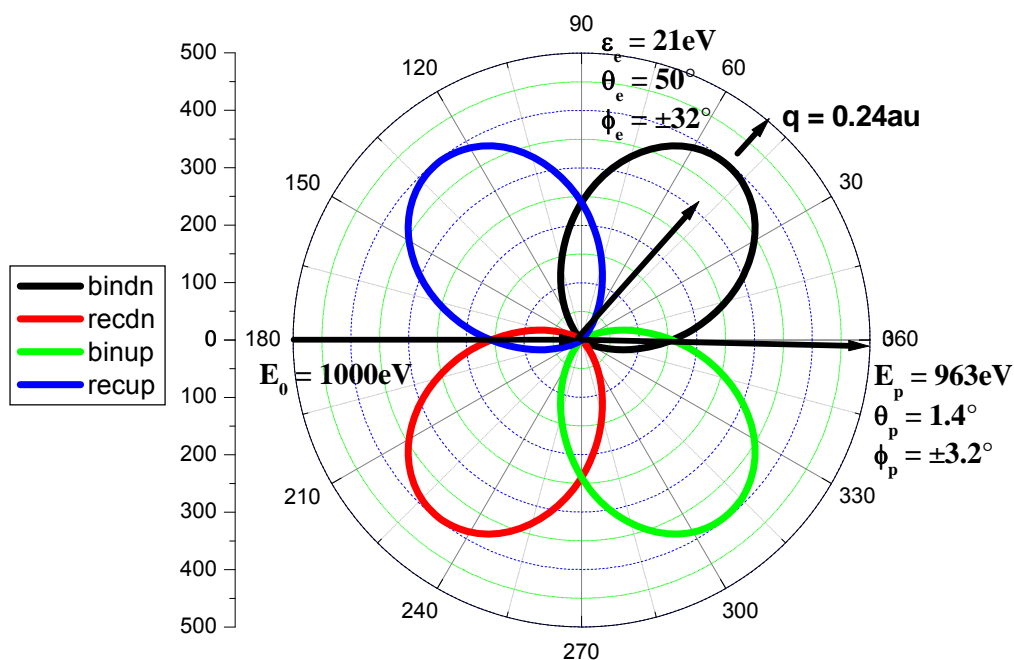
Figure 3.15.   Momentum Transfer Lobes.

This figure displays the cosine squared lobes used in Figure 3.16. The black (binary) and red (recoil) lobes correspond to "scatter down" projectiles and the green (binary) and blue (recoil) lobes correspond to "scatter up" projectiles. For an incoming and scattered projectile shown by the horizontal arrows, the black binary lobe is aligned along the momentum transfer axis (short black arrow) and the red recoil lobe is directly opposite. An upward scattered projectile would produce the green and blue binary and recoil lobes.

In Figure 3.16, the solid lines are the input lobes (Fig. 3.15) that have been convoluted with experimental conditions to produce the "binary measured" and "recoil measured" distributions shown by the squares. This figure contains no actual data and is

only meant to illustrate experimental effects. The convolution has artificially lowered the

intensity near the far observation angles causing the binary lobe to appear to have a larger

emission angle, θ_e, and to be narrower than the source distributions. Also the electron

PSD is blind to emission at less than 45° and greater than 135°. Because the energy is

high with respect to the extraction field, there are no contributions from turned around

electrons as illustrated in Figure 2.6.
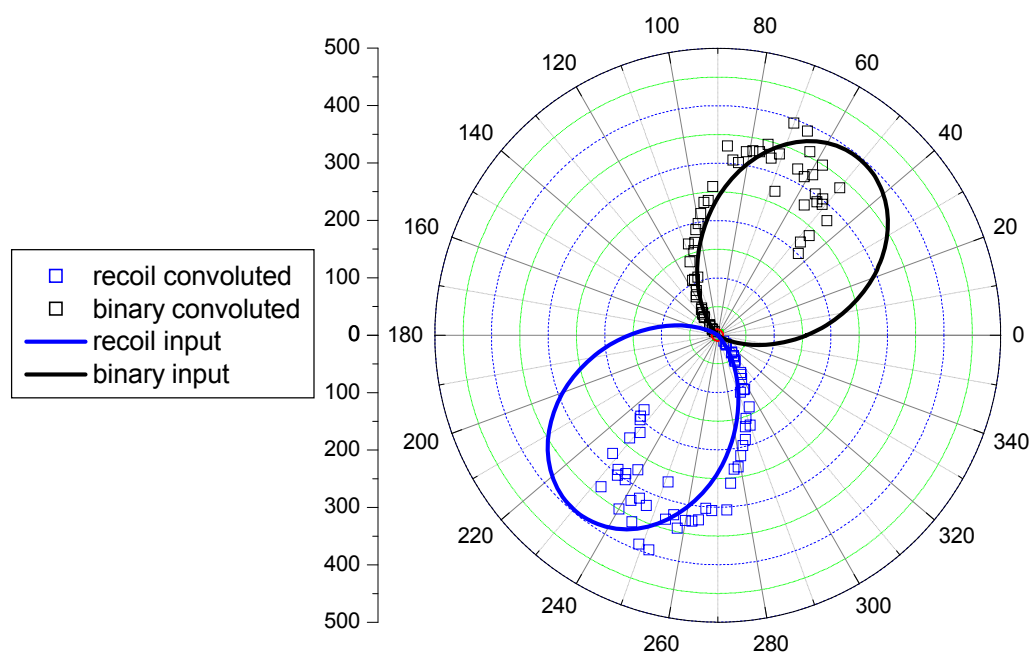
Figure 3.16.   Convolution of 21eV Lobes.

This figure displays the binary and recoil lobes from Figure 3.15 "before" (the solid lines) and "after" (the open squares) they are convoluted by the fortran program that is used to simulate the electric field and solid angle effects of the apparatus.

Figures 3.17 and 3.18 contain positron (empty circles) and electron (solid squares)

induced emission along with a convolution of input lobes that have been summed over

the full scattering and energy range. Also, shown in Figure 3.17 are the integrated input

lobes. The magnitude of momentum transfer, q, was calculated using the mean energy and scattering angle for in-plane, φ_p, $\varphi_e = 0$, scattering and the direction is indicated by the black arrow. Positron impact induced emission intensity has been scaled by a factor of 3.9 as a result of the raw single ionization P1 statistics because positron and electron impact total single ionization cross sections are equal. See the appendix for tables of the background subtracted data.

In both energy ranges and for both projectiles, the binary to recoil intensity ratios are shown to increase with increasing scattering angle and momentum transfer. No definitive differences in regards to the binary to recoil ratio between positron and electron impact are observed outside of error bars. Also, as expected for intermediate momentum transfer, 0.2 **Error! Bookmark not defined.**$\leq q \leq 1$ a.u., the symmetry of the recoil lobe no longer coincides with the momentum transfer direction [1].

With respect to differences between positron and electron impact emission, positron impact yields higher binary intensity in agreement with theory [55], though larger recoil intensity for positron emission is shown as well. Fitting parameters, not shown, also suggest a broader recoil lobe for positron impact suggesting different charge effects with respect to projectile-ion interactions. These parameters also indicate a forward shift of binary emission for positron impact and differing recoil lobe centers.
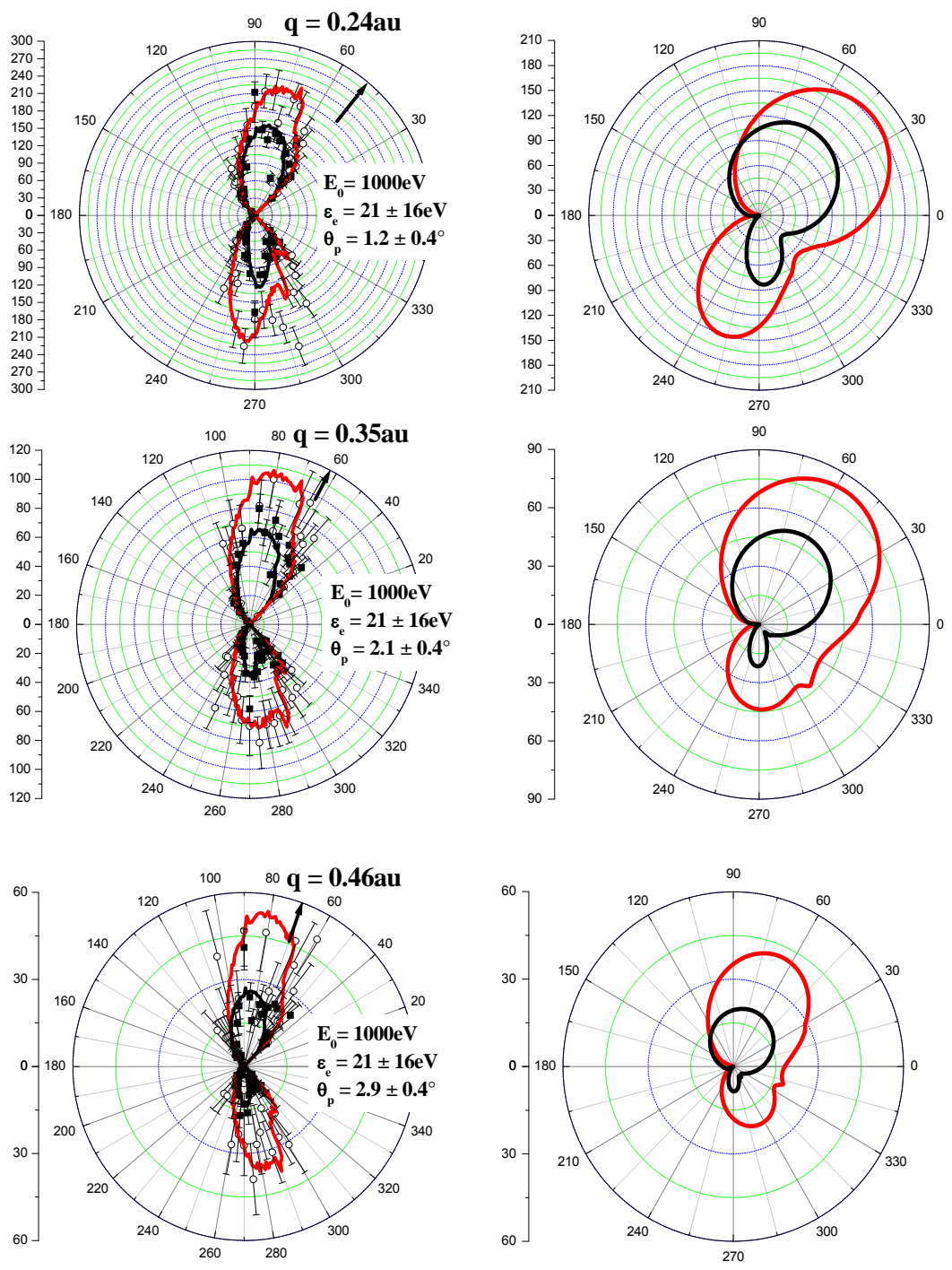
Figure 3.17. Emission 1-1, 1-2, and 1-3.

This figure displays the triply differential emission for positron (empty circles) and electron (solid squares). Data are for energy loss range 1, 21±16 eV and three scattering angles. The input (right figures) and convoluted (left figures) binary and recoil lobes are shown by solid lines for positron (red) and electron (black) impact. The input lobes were adjusted in order to achieve best fit with the data.
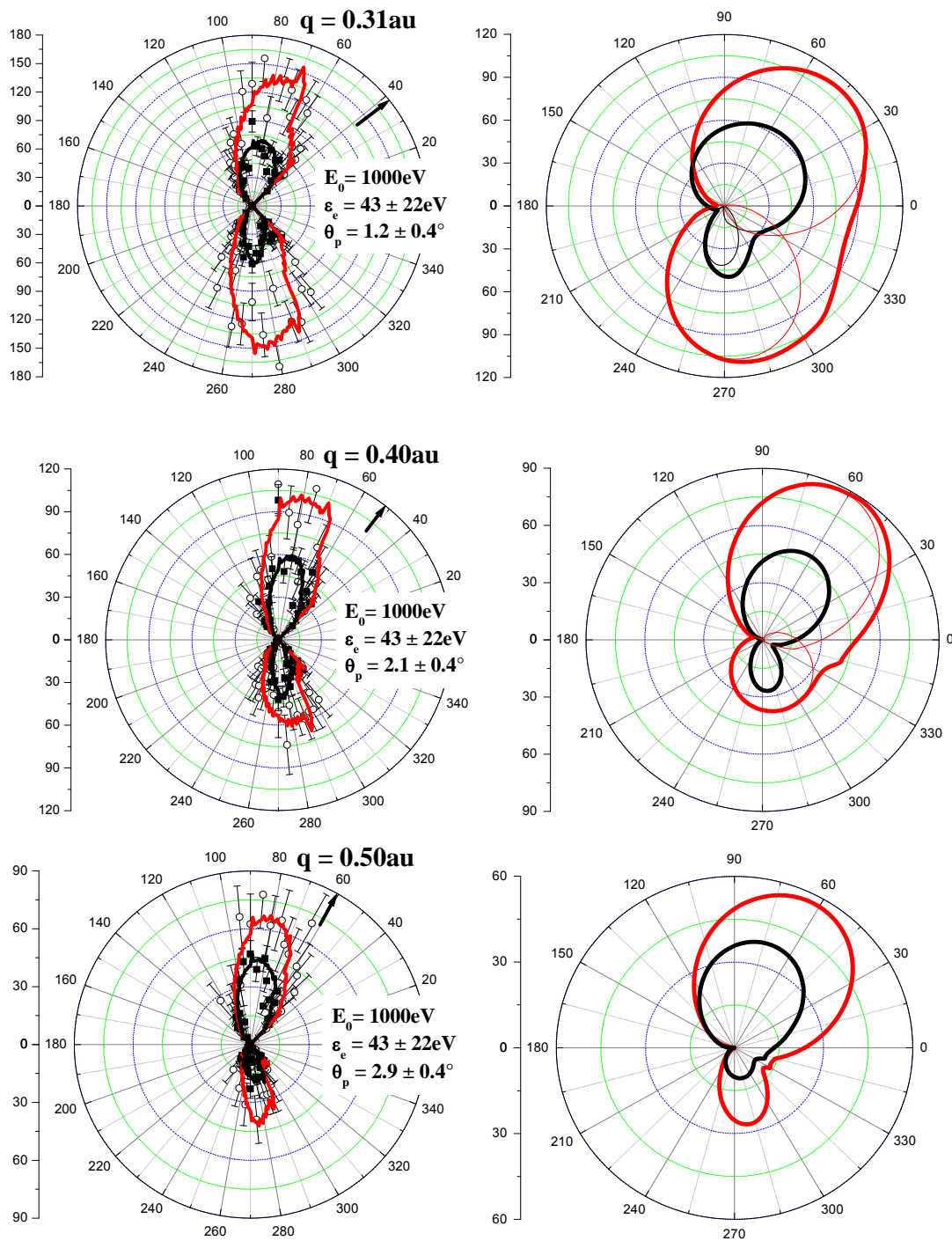
Figure 3.18. Emission 2-1, 2-2, and 2-3.

Same of Fig. 3.15 but for energy loss range 2, 43±22 eV. Again the input lobes were adjusted in order to provide best fit with the data.

3.5.   MULTIPLE IONIZATION

In contrast to earlier positron impact studies, the present method allows us to go beyond single ionization and to obtain differential information for multiple ionization as well. More importantly, because we can measure how much energy is lost in the collision, we know that we observe multiple ionization only of the outer shell of argon. However, the extent to which multiple ionization can be examined is limited by low statistics. Also, in order to examine the features as sensitively as possible, multiple to single ionization ratios are used.

3.5.1.   Projectile R2 Ratios. Analysis of P2 coincidences was performed in the same fashion as the P1E1 to P1 ratios replacing the P1E1 divided by P2 (Fig. 3.19). R2 ratios (P2/P1) were taken for the projectile P2 analysis at 46, 79, and 112 eV energy loss and included 15 channels per slice for increased statistics. These ratios compare the scattering behavior of double ionization to single ionization scattering as a function of energy loss. According to K. Paludan [37], R2 ratios for electron and positron impact are reported as approximately 0.06 and 0.04, respectively. In order to establish a basis of comparison between electron and positron impact ratios, the raw statistics (Table 3.1) and the values reported by K. Paludan have been used to calculate a scaling factor for the R2 ratios. The scaling factors were 0.9 and 2 for electron and positron impact, respectively. Solid (electron impact) and dashed (positron impact) horizontal lines have been inserted into the plots at R2 = 0.06 and 0.04. Therefore, the lines represent R2 ratios in which double ionization scattering behavior is identical to single ionization at the appropriate magnitude.

The projectile scattering R2 ratios suggest that projectile scattering for double ionization approaches a more single ionization behavior, evidenced by a more constant

ratio, as the mean energy loss increases implying a shift from single projectile interactions, i.e., TS1 and SO, to more double projectile interactions, i.e., TS2. While these differences could also be related to single ionization post collision interactions, these effects are assumed to be minimal since the measurements include a broad range of energies and large scattering angles. Both ratios show the same overall scattering dependency and, unexpectedly, similar magnitudes with a few asymmetrical exceptions. At 46 eV and 76 eV, double ionization favors larger scattering angles, i.e. less small angle-scattering at 46 eV and more large angle-scattering at 76 eV than single ionization.
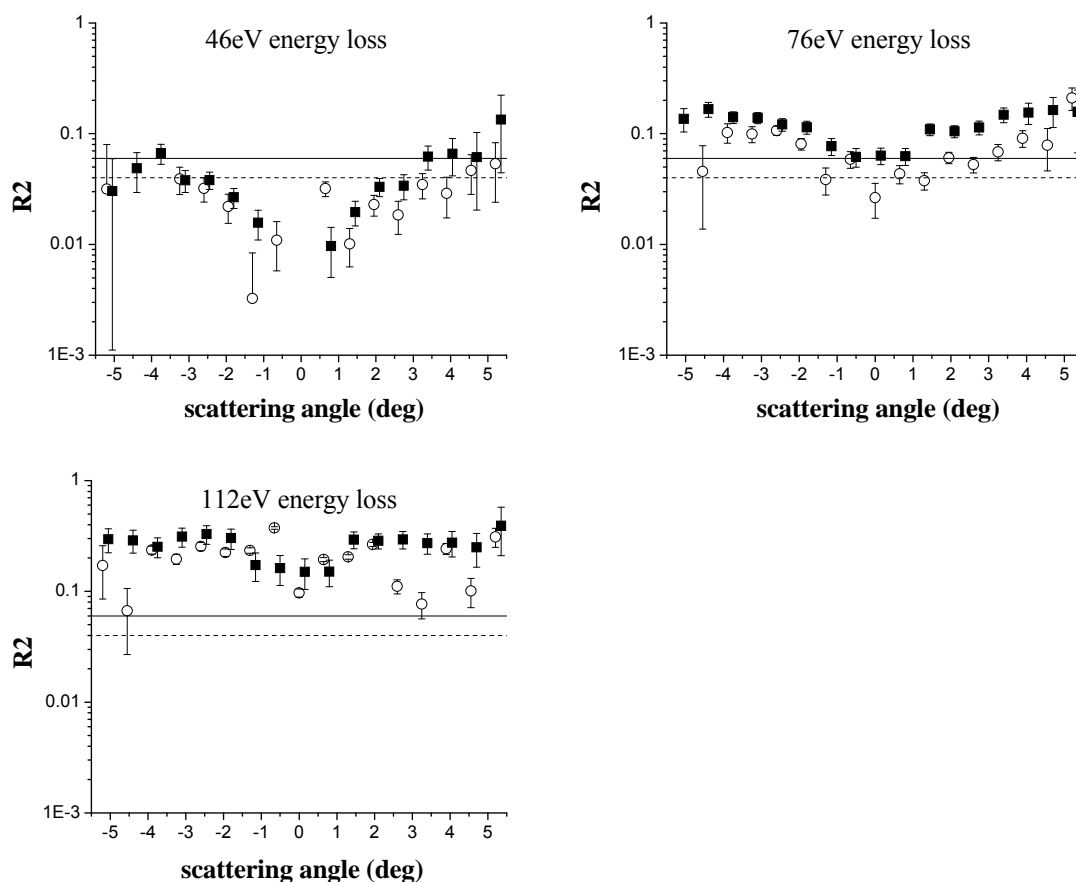
Figure 3.19. Projectile Scattering R2 Ratios.

Projectile R2 ratios for positron (empty circles) and electron (solid squares) impact at various projectile energy losses with respect to scattering angle. The solid and dashed horizontal lines represent the total cross section R2 ratios [37] of electron and positron impact, respectively.

3.5.2.   Double Ionization Electron Emission Comparisons. While the previous comparisons give insights mainly into the scattering behavior of the projectile, they are only half of the picture. Electron emission coincidences non inclusive of projectile coincidences were also recorded and analyzed. The various types of emission spectra include E1, E2, E3, E1P1, and E2P2. E1P1 and E2P2 are the corresponding emission spectra of the P1E1 and P2E2 projectile spectra mentioned above, respectively. The emission spectra were sorted by projecting 2D, 66 channel wide regions centered and symmetric about the beam direction into 1D spectra (Fig. 3.3). The width of the region equates to a straight trajectory, out-of-plane emission of approximately 32°. The spectra were binned by 5 channels. R2 (E2/E1) and R3 (E3/E1) ratios were calculated comparing single ionization emission to double and triple ionization emission, respectively. The E1, E2, and E3 spectra are the integral of emission over all projectile scattering angles and energy losses whereas the E1P1 and E2P2 spectra are integral over the projectile scattering angles and energies in coincidence with emission. The emission ratios are shown in Figure 3.25. The data was fit with a 2nd degree polynomial using error as a weighting factor through the expression $1/error^2$. According to Bluhme [5] the total single ionization cross sections at 1 keV for electron and positron impact on argon are effectively equal. However, definite differences between electron and positron impact can be found in the doubly differential R2 ratios. The mean of the R2 ratios are 0.16 ± 0.02 (electron impact) and 0.08 ± 0.02 (positron impact) which are in agreement with interference expectations. The mean of the R3 ratios are 0.038 ± 0.014 (electron impact) and 0.014 ± 0.015 (positron impact).
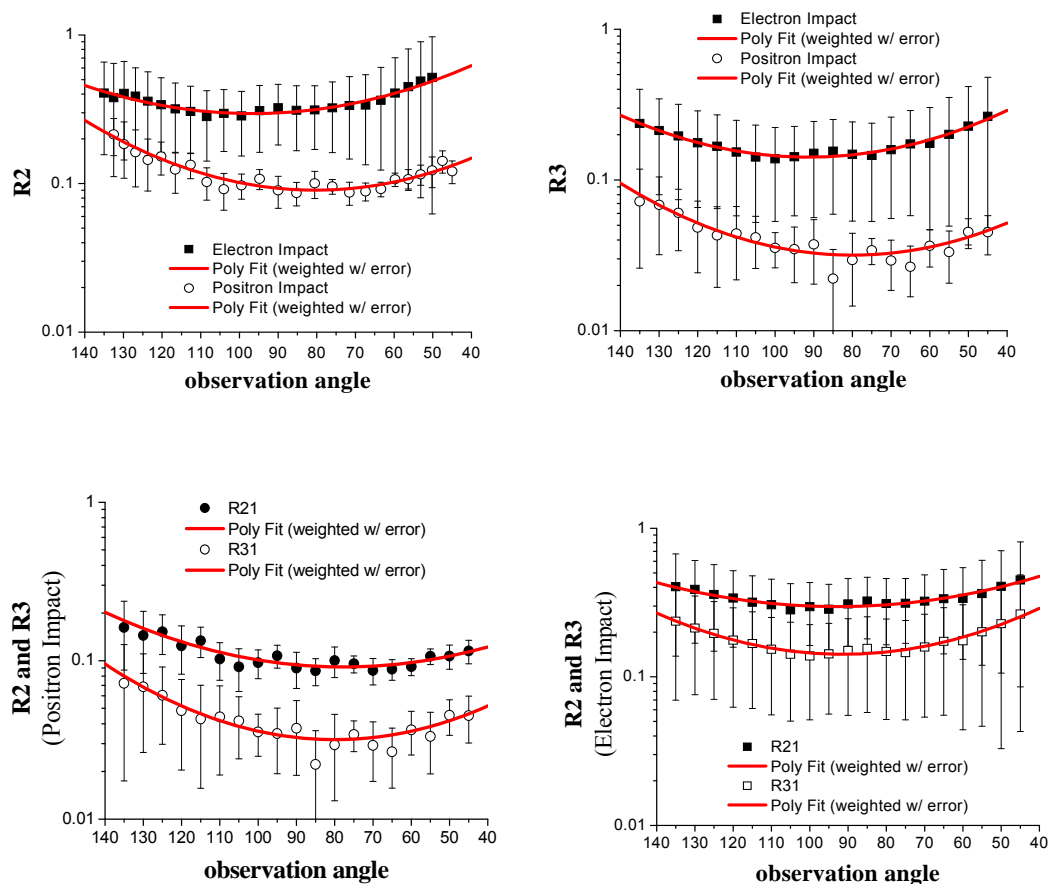
Figure 3.20. R2 and R3 Emission Ratios.

This figure compares R2 and R3 emission ratios for positron (empty circles) and electron (solid squares) impact. The red lines are polynomial fits of the ratios weighted with error. In the top plots, the ratios are grouped together according to their type and, in the bottom plots, the ratios are grouped together according to the projectile.

3.5.3. Triply Differential Multiple to Single Ionization Ratios. In Table 3.2, the total coincidences for TD single and double ionization measurements are displayed for electron and positron impact and have been divided into binary and recoil coincidences. The corresponding background is given in parenthesis. Ratios of double to single ionization are displayed along with a statistical error calculated using the method

above. The coincidences were sorted as in the example given in Figure 3.7, except that

the totals were summed before projecting. Coincidences corresponding to projectiles

scattering from 0° to -5° (+5°) are included in the binary (recoil) totals.

Binary and recoil ratios are within the margins of error for each projectile, though

positron impact shows a slightly larger recoil occurrence and electron impact shows a

larger binary occurrence in regards to a double to single ionization comparison.

Table 3.2.   Triply Differential Emission R2 Ratios.

This figure compares the triply differential emission R2 ratios of electron and positron impact
with respect to binary and recoil interactions.

	Positron Impact			Electron Impact		
	Single Ionization	Ratio	Double Ionization	Single Ionization	Ratio	Double Ionization
Recoil	5471 (69)	0.0256 ± 0.0051	140 (10)	17772 (5372)	0.125 ± 0.010	2219 (4942)
Binary	5432 (54)	0.0221 ± 0.0013	120 (10)	19212 (5701)	0.138 ± 0.010	2646 (4532)

In Figure 3.21, the triply differential R2 ratio is shown with respect to emission

angle for both projectiles. These ratios were generated in the same manner as the example

in Figure 3.7, except that all emission has been included regardless to projectile

conditions. Although each ratio is within error bars of the other and both seem to have

the same angular dependence, double ionization is shown to be less probable for positron

impact.
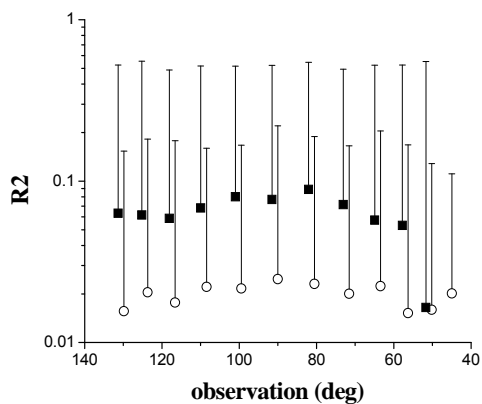
Figure 3.21. Triply Differential Emission R2 Ratio.

Triply differential measurement of R2 for electron (solid squares) and positron (empty circles) impact. Ratios for double to single ionization are shown versus the observation angle.

CONCLUSIONS

In search of charge related kinematical differences, information for 1000 eV positron induced ionization of Ar has been presented in direct comparison to electron impact ionization. Previously observed differences have been attributed to post-collision effects, target polarization and the interference between different double ionization mechanisms. Doubly and triply differential projectile information shows a larger shift of ionization intensity towards higher energies at large scattering angles for electron impact single ionization than for positron impact. Furthermore, positrons show more binary scattering at all observed energy ranges with respect to electron projectile scattering.

Triply differential emission distributions comparing binary and recoil lobe features for positron and electron impact single ionization have been generated for varying emission energy and projectile scattering angle. Though no conclusive differences are seen with respect to binary to recoil ratios, a fitting parameter suggest broader recoil lobes and more forward shifted binary lobes for positron impact. Positron impact is also shown to produce larger binary and recoil intensities.

Multiple ionization was probed using doubly differential R2 ratios of projectile scattering and doubly differential R2 and R3 emission ratios. The R2 projectile scattering ratios suggest that projectile scattering for double ionization approaches the single ionization behavior as the energy loss increases which means that the TS1 double ionization mechanism becomes dominant. As for emission R2 and R3 ratios, positron impact shows a reduction in forward emission and an enhancement in backward emission in comparison to electron impact. The reduction in forward emission implies post-collision attraction of the ejected electron to the positron projectile. The enhancement of

backward emission could arise from many body effects of the target nucleus. Triply differential R2 ratios were determined with respect to binary and recoil interactions and were also presented with respect to emission observation angle. These ratios showed no preference as to binary or recoil interactions for both projectiles and both projectiles produced similar emission angle dependencies for triply differential R2 ratios.

In future studies, experiments of this type can be improved in two ways; increased resolution and statistics. For positron impact, both can be addressed through a higher beam rate in that resolution can be improved by simply using smaller apertures and a narrower spectrometer slit entrance. However, this is exactly where the difficulty lies with positron experiments because of difficulties mentioned above. Two factors are believed to be responsible for the poor moderator efficiency used for this experiment, namely contamination and insufficient heat. Assuming that rare gas moderators and increasing the source strength are not an option, perhaps the best approach to improving the moderator efficiency is using induction for tungsten moderator production. Minimum contact with the tungsten sample could be used, thus reducing contamination and allowing free heat expansion of the sample. Also, containment of and delivery of power to the sample would not place any minimum requirements, past what traditional high vacuum techniques would impose, on the amount of vacuum space, therefore, lowering the obtainable pressure and the manageability of the vacuum.

It was observed that a higher resolution was achieved with this type of energy spectrometer as the impact energy was lowered. Therefore, floating the spectrometer to a higher potential would have the same effect for higher impact energies. However, this will alter the scattering angles and decrease the maximum detectable energy loss.

While using an extraction field and having to calibrate emission angles is undesirable, accurate results can be obtained as long as the emission energy is accurate and precise. Also, using an extraction field simplifies the electronic timing as opposed to a pulsed extraction.

Aside from a better moderator, statistics can be increased by using larger detectors or, though adding extensive electronics, an arrangement of detectors. Moving the detectors closer to the interaction region would increase their observation solid angle, but possibly increase the "random" to "real" ratio or worse, damage a detector through close proximity to the beam.

Finally, if a high positron beam rate is unobtainable, the apparatus should be designed such that an electron beam is exposed to as much of the same beamline for positrons as possible and such that the projectile can be switched without breaking vacuum and altering the apparatus. This would not only provide convenience and reliability/quality of the data, but would also make the calibration of the transport parameters and detector electronics easier considering that the electron beam rate is practically unlimited through the use of an electron gun.

APPENDIX

TDCS Experimental Data of Figure 17. Energy; 21±16 eV.

	Positron Impact							Electron Impact					
	Binary				Recoil			Binary				Recoil	
θ_e	θ_p= 1.2, 2.1, 2.9			θ_e	θ_p= 1.2, 2.1, 2.9			θ_e	θ_p= 1.2, 2.1, 2.9			θ_e	θ_p= 1.2, 2.1, 2.9	
135	0	0	0	225	0	0	0	135	0	0	0	225	1	0	0
133	1	0	0	227	3	1	0	133	9	3	1	227	7	5	1
130	9	2	0	230	6	2	0	130	25	11	4	230	21	8	4
127	8	3	4	233	14	7	3	127	39	18	5	233	41	11	2
124	16	4	3	236	14	7	1	124	44	11	4	236	32	10	2
120	17	5	3	240	18	1	3	120	42	19	6	240	28	15	3
117	23	4	3	243	21	10	1	117	40	21	8	243	39	14	5
113	16	4	3	247	35	16	2	113	49	24	4	247	36	13	6
108	23	15	5	252	27	10	2	108	80	31	8	252	48	17	6
104	30	14	10	256	31	13	3	104	91	42	4	256	71	20	3
99	32	18	5	261	51	13	7	99	84	49	15	261	76	22	10
95	40	17	6	265	58	17	6	95	132	56	21	265	101	34	17
90	48	31	12	270	46	18	7	90	212	122	41	270	167	58	13
85	55	21	17	275	42	21	10	85	148	80	24	275	103	36	16
81	56	26	12	279	47	18	7	81	132	64	16	279	103	33	10
76	42	17	4	284	51	18	6	76	145	74	22	284	72	22	8
72	54	31	7	288	61	17	8	72	135	64	19	288	75	26	6
67	52	23	12	293	37	17	4	67	69	37	22	293	49	12	4
63	34	24	10	297	38	13	7	63	119	61	24	297	80	21	7
60	43	18	13	300	45	15	8	60	141	53	23	300	73	33	9
56	38	17	8	304	32	9	5	56	106	50	14	304	55	33	9
53	25	19	5	307	28	14	1	53	74	35	14	307	51	23	5
50	28	12	5	310	24	9	3	50	75	43	13	310	48	35	12
47	22	9	3	313	24	11	1	47	91	53	24	313	63	29	9
45	14	2	3	315	8	4	1	45	42	29	11	315	37	16	4

TDCS Experimental Data of Figure 18. Energy; 43±22 eV.

	Positron Impact							Electron Impact						
	Binary				Recoil				Binary				Recoil		
θ_e	θ_p= 1.2, 2.1, 2.9			θ_e	θ_p= 1.2, 2.1, 2.9			θ_e	θ_p= 1.2, 2.1, 2.9			θ_e	θ_p= 1.2, 2.1, 2.9		
135	0	0	0	225	0	0	0	135	0	0	0	225	0	0	0
133	1	0	1	227	1	1	2	133	1	1	1	227	1	2	1
130	5	6	12	230	6	3	9	130	10	12	5	230	10	9	2
127	7	2	16	233	7	6	8	127	22	16	11	233	22	8	7
124	9	9	16	236	10	3	12	124	15	16	10	236	25	12	9
120	9	3	14	240	16	6	5	120	23	14	12	240	19	5	5
117	13	4	30	243	11	9	7	117	24	30	16	243	16	7	5
113	12	2	15	247	24	9	14	113	27	15	4	247	24	14	7
108	18	12	23	252	13	11	15	108	28	23	17	252	29	15	12
104	20	13	27	256	18	9	20	104	45	27	12	256	41	20	9
99	17	11	38	261	33	5	30	99	42	38	34	261	55	30	11
95	31	15	50	265	32	10	29	95	40	50	43	265	43	29	14
90	33	28	98	270	26	13	42	90	89	98	47	270	61	42	23
85	40	23	48	275	35	19	40	85	63	48	39	275	50	40	8
81	24	21	58	279	44	12	27	81	61	58	45	279	51	27	17
76	35	28	57	284	23	14	34	76	54	57	34	284	40	34	9
72	33	11	50	288	33	15	18	72	62	50	21	288	35	18	3
67	26	18	26	293	34	14	19	67	39	26	25	293	23	19	13
63	32	14	53	297	10	14	25	63	54	53	31	297	42	25	3
60	29	10	39	300	26	11	24	60	56	39	25	300	40	24	13
56	19	12	29	304	28	13	27	56	42	29	16	304	37	27	10
53	17	10	23	307	19	5	17	53	33	23	17	307	21	17	8
50	20	8	34	310	12	1	27	50	40	34	16	310	39	27	11
47	17	7	34	313	11	6	20	47	43	34	14	313	45	20	8
45	12	3	14	315	11	2	10	45	22	14	0	315	24	10	0

BIBLIOGRAPHY

[1] H. Ehrhardt, K. Jung, G. Knoth, and P. Shlemmer, Z. Phys. D **1**, 3 (1986).

[2] A. Kover and G. Laricchia, Phys. Rev. Lett. **80**, 5309 (1998).

[3] M. Charlton, Rep. Prog. Phys. **48**, 737 (1985).

[4] D. Fromme, G. Kruse, W. Raith, and G. Sinapius, Phys. Rev. Lett. **57**, 3031 (1986).

[5] T. Falke, T. Brandt, O. Kuhl, W. Raith and M. Weber, J. Phys B **30**, 3247 (1997).

[6] A. Schmitt, U. Cerny, H. Möller, W. Raith, and M. Webber, Phys. Rev. A **49**, R5 (1994).

[7] A. Kover, R. M. Finch, M. Charlton, and G. Laricchia, J. Phys. B **30**, L507 (1997).

[8] A. Kover, G. Laricchia, and M. Charlton, J. Phys. B **27**, 2409 (1994).

[9] R. G. Greaves and C. M. Surko, Phys. Plasmas **4**, 1528 (1997).

[10] H. Bluhme, H. Knudsen, J. P. Merrison, and K. A. Nielsen, J. Phys. B **32**, 5835 (1999).

[11] H. Bluhme, H. Knudsen, J. P. Merrison, and K. A. Nielsen, J. Phys. B **32**, 5237 (1999).

[12] G. Laricchia, P. Van Reeth, M. Szluinska, and J. Moxom, J. Phys. B **35**, 2525 (2002).

[13] J. Moxom, G. Laricchia, and M. Charlton, J. Phys. B: At. Mol. Opt. Phys. **28**, 1331 (1995).

[14] G. Kruse, A. Quermann, W. Raith, G. Sinapius, and M. Weber, J. Phys. B **24**, L33 (1991).

[15] J. Moxom, G. Laricchia, and M. Charlton, J. Phys. B **26**, L367 (1993).

[16] F. M. Jacobsen, N. P. Frandsen, H. Knudsen, U. Mikkelsen, and D. M. Schrader, J. Phys. B **28**, 4691 (1995).

[17] V. Kara, K. Paludan, J. Moxom, P. Ashley, and G. Laricchia, J. Phys. B **30**, 3933 (1997).

[18] K. Paludan, G. Laricchia, P. Ashley, V. Kara, J. Moxomy, H. Bluhme, H. Knudsen, U. Mikkelsen, S. P. Møller, E. Uggerhøj, and E. Morenzoni, J. Phys. B **30**, L581 (1997).

[20] J. Moxom, D. M. Schrader, G. Laricchia, L. Xu, and L. D. Hulett, Phys. Rev. A **60**, 2940 (1999).

[21] G. Spicher, B. Olsson, W. Raith, G. Sinapius, and W. Sperber, Phys. Rev. Lett. **64**, 1019 (1990).

[22] A. Hofmann, T. Falke, W. Raith, M. Weber, D. Becker, and K. G. Lynn, J. Phys. B **30**, 3297 (1997).

[23] C. M. Surko, G. F. Gribakin, and S. J. Buckman J. Phys. **38**, R57 (2005).

[24] H. Knudsen and J. F. Reading, Phys. Rep. **212**, 107 (1992).

[25] J. Moxom, G. Laricchia, M. Charlton, G. O. Jones and A. Kover, J. Phys. B **25,** L613 (1992).

[26] A. Kover, G. Laricchia, and M. Charlton, J. Phys. B **26**, L575 (1993).

[27] K. Bartschat, Phys. Rev. A **71**, 032718 (2005).

[28] S. A. Novikov, J. W. J. Bromley, and J. Mitroy, Phys. Rev. A **69**, 052702 (2004).

[29] R. I. Campeanu, L. Nagy, and A. D. Stauffer, Can. J. Phys. **81**, 919 (2003).

[30] E. G. Cavalcanti, G. M. Sigaud1,E. C. Montenegro1, and H. Schmidt-Böcking Phys. Rev. Lett. **22**, 3087 (2003).

[31] J. H. McGuire, Phys. Rev. Lett. **49**, 1153 (1982).

[32] L. H. Anderson, P. Hvelplund, H. Knudsen, S. P. Moller, A. H. Sorensen, K. Elsener, K. G. Rensfelt, E. Uggerhoj, Phys. Rev. A **36**, 3612 (1987).

[33] M. Charlton, J. Phys. B **21,** L545 (1988).

[34] S. Helms, U. Brinkmann, J. Deiwiks, R. Hippler, D. Segers, and J. Paridaens, J. Phys. B **27**, L557 (1994).

[35] R. Hippler, S. Helms, U. Brinkmann, J. Deiwiks, H. Schneider, and D. Segers, Can. J. Phys. **74**, 373 (1996).

[36] S. Helms, U. Brinhann, J. Deiwiks, R. Hippler, H. Schneider, D. Segers, and J. Paridaensgs, J. Phys. B **28**, 1095 (1995).

[37] K. Paludan, H. Bluhme, H. Knudsen, U. Mikkelsen, S. P. Møller, E. Uggerhøj, and E. Morenzonix, J. Phys. B **30**, 3951 (1997).

[38] R. D. DuBois, C. Doudna1, C. Lloyd1, M. Kahveci1, Kh. Khayyat1, Y. Zhou1, and D. H. Madison, J. Phys. B **34**, L783 (2001).

[39] D. R. Schultz, L. Meng, and R. E. Olson, J. Phys. B **25**, 4601 (1992).

[40] R. M. Finch, A. Kover, M. Charlton, and G. Laricchia, J. Phys. B **29**, L667 (1996).

[41] L. Dou L, W. E. Kauppila, C. K. Kwan, D. Przybyla, S. J. Smith, and T. S. Stein, Phys. Rev. A **46**, R5327 (1992a).

[42] L. Dou, W. E. Kauppila, C. K. Kwan, and T. S. Stein, Phys. Rev. Lett. **68**, 2913 (1992b).

[43] O. G. de Lucio, J. Gavin, and R. D. DuBois, Phys. Rev. Lett. **97**, 243201 (2006).

[44] J. Moxom, G. Laricchia, M. Charlton, G. O. Jones, and A. Kover, J. Phys. B **25**, L613 (1992).

[45] D. E. Golden, Z. Xu, J. Bernhard, and D. W. Mueller, J. Phys. B **29**, 3741 (1996).

[46] P. Guang-yan, P. Hvelplund, H. Knudsen, Y. Yamazaki, M. Brauner, and J. S. Briggs, Phys. Rev. A **47**, 1531 (1992).

[47] G. B. Crooks and M. E. Rudd, Phys. Rev. Lett. **25**, 1599 (1970).

[48] M. Rodbro and F. D. Andersen, J. Phys. B **12**, 2883 (1979).

[49] H. Knudsen, L. H. Andersen, and K. E. Jensen, J. Phys. B **19**, 3341 (1986).

[50] A. Salin, J. Phys. B **2**, 631 (1969).

[51] J. Macek, Phys. Rev. A **1**, 235 (1970).

[52] P. Mandal, K. Roy, and N. C. Sil, Phys. Rev. A **33,** 756 (1986).

[53] D. R. Schultz and C. O. Reinhold, J. Phys. B **23**, L9 (1990).

[54] R. A. Sparrow and R. E. Olson, J. Phys. B **27**, 2647 (1994).

[55] Sadhanna Sharma and M. K. Shrivastava, Phys. Rev. A **38**, 2 (1988).

[56] K. Jung, R. Muller-Fiedler, P. Schlemmer, H. Ehrhardt, and H. Klar, J. Phys. B **18**, 2955 (1985).

[57] M. Brauner, J. S. Briggs and H. Klar, J. Phys. B **22**, 2265 (1989).

[58] A. Kover, K. Paludan, and G. Laricchia, J. Phys. B **34**, L219 (2001).

[59] J. Fiol, V. D. Rodrıguez, and R. O. Barrachina, J. Phys. B **34**, 933 (2001).

[60] O. G. de Lucio, R. D. DuBois and J. Gavin, J. of Phys.: Conf. Ser. **88**, 012063 (2007).

[61] P. Bolognesi, H. Bohachov, V. Borovik, S. Veronesi, R. Flammini, E. Fainelli, A Borovik, J. Martinez, Colm T. Whelan, H. R. J. Walters, A. Kheifets, and L. Avaldi, J. Phys. B **41**, 015201 (2008).

[62] S. Knoop, D. Fischer, Y. Xue, M. Zapukhlyak, C. J. Osborne, Th. Ergler, T. Ferger, J. Braun, G. Brenner, H. Bruhns, C. Dimopoulou, S. W. Epp, A. J. Gonzalez Martınez, G. Sikler, R. SoriaOrts, H. Tawara, T. Kirchner, J. R. Crespo Lopez-Urrutia, R. Moshammer, J. Ullrich, and R. Hoekstra, J. Phys. B **41**, 195203 (2008).

[63] P. Bolognesi, L. Pravica, S. Veronesi, E. Fainelli, L. Avaldi, and K. Bartschat, J. Phys. B **41**, 065203 (2008).

[64] F. Afaneh, L. Ph. H. Schmidt, M. Schoffler, K. E. Stiebing, J. Al-Jundi, H. Schmidt-Bocking, and R. Dorner, J. Phys. B **40**, 3467 (2007).

[65] B. Najjari, N. Lahmidi, A. Dorn, and B. Joulakian, J. Phys. B **40**, 157 (2007).

[66] A. Naja, E. M. Staicu-Casagrande, A. Lahmam-Bennani, M. Nekkab, F. Mezdari, B. Joulakian, O. Chuluunbaatar, and D. H. Madison, J. Phys. B **40**, 3775 (2007).

[67] N.V. Maydanyuk, A. Hasan, M. Foster, B. Tooke, E. Nanni, D. H. Madison, and M. Schulz, Phys. Rev. Lett. **94,** 243201 (2005).

[68] llham Taouil, Alain Duguet, Azzedine Lahmam-Bennani, Birgit Lohmann, Jens Rasch, Colm T. Whelank and H. R. James Walters, J. Phys. B **32**, L5 (1999).

[69] M. Rieth, Forschungszentrum Karlsruhe GmbH, "Creep and Recrystallization of Pure and Dispersion Strengthened Tungsten,**"** Institut für Materialforschung I, (2005).

[70] M. Greiner and P. Kruse, Rev. of Sci. Instrs. **78**, 026104 (2007).

[71] Yasuyuki Nagashima, Toshikazu Kurihara, Fiminori Saito, Yoshiko Itoh, Akira Goto, and Toshio Hyodo, Jpn. J. of Appl. Phys. **39**, 5356 (2000).

[72] H. M. Weng Nuc. Instrs. and Meth. in Phys. Res. B **225**, 397 (2004).

[73] Makoto Muramatsu, Toshiyuki Ohdaira, and Ryoichi Suzuki, Jpn. J. of Appl. Phys. **44**, 6283 (2005).

[74] William D. Klopp and Peter L. Raffo, NASA Technical Note D-2503, (1964).

[75] William D. Klopp and Walter R. Witzke, NASA Technical Note D-3232 (1966).

[76] A. Goodyear, A. P. Knights, and P. G. Coleman, I. Phys.: Condens. Matter **6,** 9601 (1994).

[77] R. G. Carlson, J. of the Electrochemical Soc. **106**, 49 (1959).

VITA

Jared Gavin was born in Arkansas on September 8, 1981. He earned a B.S. in mathematics from the University of Arkansas at Monticello in December 2004. He earned an M.S. in physics at the University of Missouri at Rolla in 2005. Under the advisement of Dr. Robert DuBois, he was awarded his Ph. D. in physics from the Missouri University of Science and Technology in the spring 2009. Jared has also coauthored several publications including a Physical Review Letter in 2006, as well as presented posters at DAMOP and UMR-SLU meetings.